biosensors

MDPI

Article

Design and Performance Analysis of an SPR Sensor for Milk Adulteration Monitoring

John Germán Vera Luzuriaga [1,*], Marco Guevara [2], Diana Coello-Fiallos [3] and Cristian Vacacela Gomez [4,*]

[1] Departamento de Ciencias de la Energía y Mecánica, Universidad de las Fuerzas Armadas ESPE, Latacunga 050150, Ecuador
[2] Facultad de Mecánica, Escuela Superior Politécnica de Chimborazo (ESPOCH), Riobamba 060155, Ecuador
[3] Carrera de Física, Grupo GIMA, Facultad de Ciencias, Escuela Superior Politécnica de Chimborazo (ESPOCH), Riobamba 060155, Ecuador
[4] Universidad Ecotec, Km. 13.5 Samborondón, Samborondón 092302, Ecuador
* Correspondence: jgvera4@espe.edu.ec (J.G.V.L.); cristianisaac.vacacelagomez@fis.unical.it (C.V.G.)

Abstract

Hydrogen peroxide (H_2O_2) may be illegally added to milk to delay visible spoilage, producing concentration-dependent changes in its refractive index. This study numerically evaluates the optical response of a B-sil/Al/Al_2O_3/WS_2 surface plasmon resonance (SPR) configuration to these refractive-index variations. The angular SPR response was calculated at λ = 633 nm using the transfer matrix method under TM-polarized illumination. The B-sil/Al/Al_2O_3/WS_2 architecture was established through sequential evaluation of prism material, Al thickness, Al_2O_3 thickness, and 2D interfacial material, followed by assessment of its response to H_2O_2-associated refractive-index changes in milk. The final structure consisted of 70 nm Al, 25 nm Al_2O_3, and 0.80 nm WS_2. Across the simulated H_2O_2 conditions, the resonance angle shifted from 85.65° to 86.11°, while the angular sensitivity ranged from 383.82 to 406.45°/RIU. The best balance among the evaluated metrics was obtained for H_2O_2-C2, with a sensitivity of 406.45°/RIU, QF of 4.65 RIU^{-1}, FoM of 436.48 RIU^{-1}, LoD of 1.23×10^{-5}, and CSF of 436.56. The WS_2-containing interface produced calculated angular shifts for small refractive-index variations in the milk sensing medium. Comparison with reported SPR systems for milk-related sensing showed a comparable angular sensitivity range, while QF and detection accuracy were limited by the broad resonance profile. These results characterize the theoretical optical response of the B-sil/Al/Al_2O_3/WS_2 multilayer under H_2O_2-associated refractive-index changes but do not establish chemical selectivity toward H_2O_2. Experimental implementation would require an appropriate selective filtering or recognition strategy, together with validation of matrix effects and practical sensing performance.

Keywords: surface plasmon resonance; hydrogen peroxide; milk adulteration; borosilicate prism; Kretschmann configuration; transfer matrix method; numerical simulation

Check for updates

Received: 27 July 2026
Revised: 27 August 2026
Accepted: 1 September 2026
Published: 4 September 2026

Copyright: © 2026 by the authors. Licensee MDPI, Basel, Switzerland. This article is an open access article distributed under the terms and conditions of the Creative Commons Attribution (CC BY) license.

1. Introduction

Milk is a widely consumed food that provides proteins, lipids, lactose, minerals, and vitamins essential for human nutrition [1–3]. Its nutrient-rich composition also makes it susceptible to microbial growth during collection, transport, and storage [4,5]. Poor refrigeration or handling can accelerate spoilage and motivate the illegal addition of preservatives such as hydrogen peroxide (H_2O_2), whose oxidizing and antimicrobial activity can delay visible deterioration while masking deficiencies in hygienic processing [6–9]. Residual

H_2O_2 may alter milk constituents and compromise product quality, making its detection relevant to food safety and adulteration control [10–15].

Several analytical approaches have been applied to preservative and adulterant detection in milk, including colorimetric, electrochemical, chromatographic, spectrophotometric, and optical methods [16–26]. Some of these techniques require reagents, sample pretreatment, trained personnel, or laboratory infrastructure [27,28]. Refractive-index-based optical sensing provides a label-free approach for liquid food matrices, and previous studies have shown that the refractive index of milk varies with the concentration of preservatives such as H_2O_2, formaldehyde, and sodium carbonate [18,25,29–31].

Surface plasmon resonance (SPR) detects refractive-index changes at a metal–dielectric interface [32–34]. In the Kretschmann configuration, p-polarized light is coupled through a prism to a thin metallic film, producing a reflectance minimum at the resonance angle [35,36]. Variations in the refractive index of the sensing medium shift this angle and provide the basis for analyte monitoring [33,37–39]. SPR performance is commonly characterized using angular sensitivity, full width at half maximum (FWHM), detection accuracy, and figure of merit, including in theoretical studies of preservative detection in milk [31,40,41].

Al/Al_2O_3 interfaces have also been investigated in plasmonic sensing systems because of their optical properties and compatibility with thin-film configurations [42,43]. Optical approaches for H_2O_2 detection have been reported using different plasmonic transduction mechanisms, including SPR imaging and surface-enhanced Raman scattering [44,45]. These studies show that aluminum-based plasmonic sensing and optical H_2O_2 detection are established research directions. The studies considered here, however, employ different material combinations, interrogation mechanisms, or sensing matrices from the B-sil/$Al/Al_2O_3/WS_2$ angular SPR configuration examined in the present work.

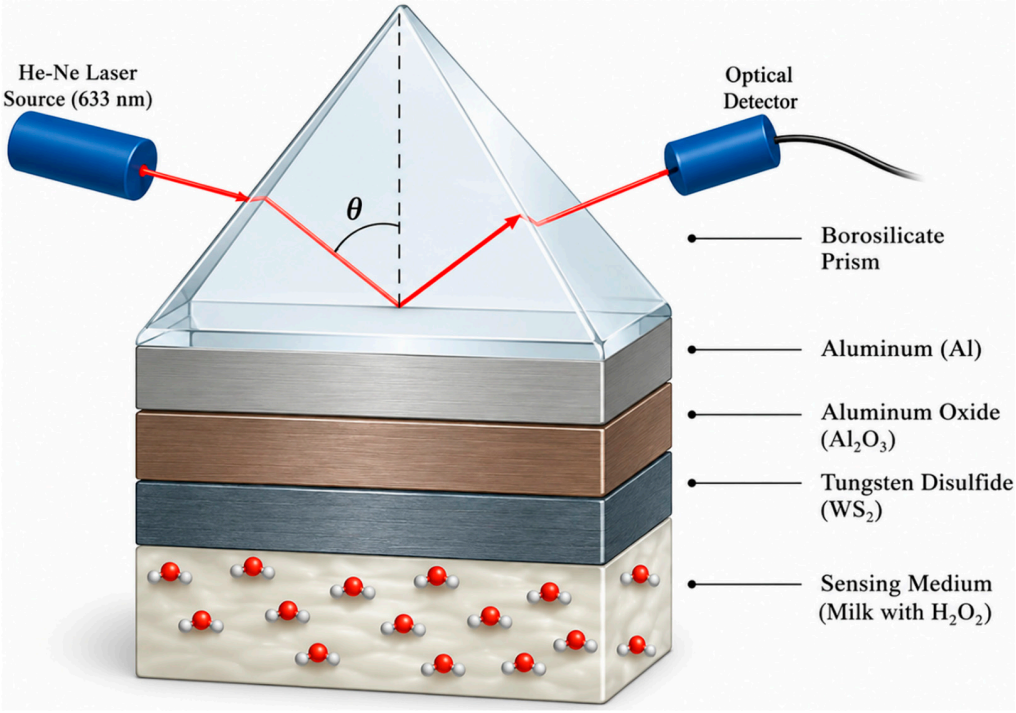
The present study therefore focuses on the numerical evaluation of a planar B-sil/$Al/Al_2O_3/WS_2$ multilayer structure in the Kretschmann configuration for monitoring refractive-index changes associated with H_2O_2 adulteration in milk. In this architecture, the borosilicate prism acts as the optical coupling element that enables phase matching between the incident wave and the surface plasmon mode [46]. Its optical transparency at the operating wavelength, mechanical stability, and compatibility with thin-film deposition support its use as the substrate for the multilayer configuration [47,48]. A thin aluminum film serves as the plasmonic layer [49], while Al_2O_3 is introduced as a dielectric coating and potential protective barrier against oxidation-related degradation of Al [50,51]. WS_2 is incorporated as a two-dimensional interfacial layer to modify the evanescent-field distribution near the sensing region and enhance the interaction between the optical field and the sensing medium [52,53]. The sensing medium is represented by milk containing H_2O_2, where concentration-dependent refractive-index variations are monitored through the corresponding displacement of the SPR angle [7,31].

The multilayer architecture is systematically evaluated through sequential analysis of prism material, Al thickness, Al_2O_3 thickness, and 2D interfacial material, followed by assessment of its angular SPR response over the modeled H_2O_2-associated refractive-index range in milk. This configuration differs from previously reported approaches in the combination of multilayer materials, angular interrogation scheme, and milk-based sensing matrix considered. The final structure is evaluated at $\lambda = 633$ nm using resonance-angle shift, angular sensitivity, FWHM, detection accuracy, figure of merit, and limit of detection. The resulting system is examined as a theoretical optical platform for H_2O_2-associated refractive-index monitoring in milk, with experimental validation required to establish its practical sensing performance.

2. Materials and Methods

2.1. Theoretical Modelling and SPR Sensor Configuration

The proposed multilayer configuration was modeled using the Kretschmann geometry for angular surface plasmon resonance interrogation. Scheme 1 shows the multilayer architecture, consisting of a borosilicate prism, an aluminum layer, an aluminum oxide coating, a tungsten disulfide interfacial layer, and the sensing medium formed by milk containing H_2O_2. A He–Ne laser source operating at λ = 633 nm was considered as the incident optical beam. The light was assumed to be transverse magnetic polarized, because only this polarization can couple efficiently with surface plasmon modes at the metal–dielectric interface. The incidence angle, θ, was varied to identify the resonance condition from the angular reflectance minimum.



Scheme 1. Proposed borosilicate prism-based SPR configuration for modeling H_2O_2-associated refractive-index changes in milk.

Table 1 summarizes the optical constants and physical thicknesses used for the final B-sil/Al/Al_2O_3/WS_2 configuration. The refractive indices correspond to the operating wavelength of 633 nm. The final metal and dielectric thicknesses were 70 nm for Al, 25 nm for Al_2O_3, and 0.80 nm for WS_2. These values were not imposed a priori; they were retained after the sequential evaluation of prism material, Al thickness, Al_2O_3 thickness, and 2D interfacial material presented in the subsequent Results subsections. The corresponding screening and optimization trends are discussed in Sections 3.1–3.6.

The metallic layer was selected as aluminum because it supports plasmonic excitation at visible wavelengths and provides a low-cost alternative to noble metals. Since aluminum is prone to surface oxidation, an Al_2O_3 coating was introduced above the Al film. In the model, this layer functions as both a dielectric spacer and a protective interface that can reduce direct degradation of the aluminum surface. The WS_2 layer was placed at the outer interface of the multilayer stack. As a two-dimensional transition-metal dichalcogenide, WS_2 modifies the evanescent-field distribution near the sensing region and increases the interaction between the optical field and the analyte-containing medium.

Table 1. Optical and geometrical parameters of the final B-sil/Al/Al_2O_3/WS_2 SPR configuration at λ = 633 nm.

Layer/Medium	Refractive Index	Thickness (nm)	Ref.
B-sil prism	1.4701	-	[42]
Al	0.0778 + 5.8535i	70	[50]
Al_2O_3	1.7700	25	[53]
WS_2	4.9000 + 0.3124i	0.80	[50]
Water medium (H_2O)	1.3300	-	[51]
Sensing medium (SM) (baseline)	1.3455	-	[52]

The sensing medium was modeled as milk adulterated with hydrogen peroxide. Changes in H_2O_2 concentration were represented through refractive-index variations relative to the baseline milk value. When the refractive index of the sensing medium changes, the phase-matching condition is altered and the SPR angle shifts. This resonance-angle displacement is the main output used to evaluate the optical response of the B-sil/Al/Al_2O_3/WS_2 configuration. The structure shown in Scheme 1 is a theoretical configuration intended for numerical analysis. Experimental implementation would require controlled deposition of the Al, Al_2O_3, and WS_2 layers, calibration with reference liquids and milk samples containing known H_2O_2 concentrations, and assessment of selectivity under realistic matrix conditions.

2.2. Numerical Modeling

The optical response of the proposed SPR configuration was evaluated using the transfer matrix method (TMM). The multilayer structure was modeled as a B-sil prism/Al/Al_2O_3/WS_2/sensing-medium stack, where each layer was defined by its refractive index, dielectric constant, and physical thickness. The TMM calculations assume planar, homogeneous, isotropic, and optically uniform layers with abrupt interfaces and fixed optical constants at the operating wavelength. Surface roughness, thickness nonuniformity, interfacial defects, and material degradation are not included in the present model.

At each interface, the tangential components of the electric and magnetic fields were assumed to be continuous. Accordingly, the field components at the first and final interfaces of the multilayer system were related through the global transfer matrix M as

$$\begin{bmatrix} E_1 \\ H_1 \end{bmatrix} = M_{ij} \begin{bmatrix} E_{N-1} \\ H_{N-1} \end{bmatrix} \quad (1)$$

where E_1 and H_1 are the tangential electric and magnetic field components at the first interface, while E_{N-1} and H_{N-1} correspond to those at the final interface. The global transfer matrix in Equation (1) was obtained from the product of the characteristic matrices of the intermediate layers, as given in Equation (2):

$$M_{ij} = \left[\prod_{k=2}^{N-1} M_k \right]_{ij} = \begin{bmatrix} M_{11} & M_{12} \\ M_{21} & M_{22} \end{bmatrix} \quad (2)$$

For TM-polarized illumination, the characteristic matrix of the kth layer was defined in Equation (3):

$$M_k = \begin{bmatrix} \cos\beta_k & (-\mathrm{i}\ \sin\beta_k)/q_k \\ -\mathrm{i}\ q_k \sin\beta_k & \cos\beta_k \end{bmatrix} \quad (3)$$

where q_k is the optical admittance and β_k is the phase thickness of the kth layer.

The optical admittance q_k and the phase thickness β_k were calculated using Equations (4) and (5), respectively:

$$\beta_k = \frac{2\pi d_k}{\lambda_0}\sqrt{\varepsilon_k - n_1^2 \sin^2\theta} \tag{4}$$

$$q_k = \frac{\sqrt{\varepsilon_k - n_1^2 \sin^2\theta}}{\varepsilon_k} \tag{5}$$

where ε_k is the dielectric constant, d_k is the layer thickness, n_1 is the refractive index of the incident medium, θ is the incident angle, and λ is the operating wavelength.

The TM reflection coefficient was calculated from the elements of the global matrix using Equation (6):

$$R = \left|\frac{(M_{11} + M_{12}\, q_N)q_1 - (M_{21} + M_{22}\, q_N)}{(M_{11} + M_{12}\, q_N)q_1 + (M_{21} + M_{22}\, q_N)}\right|^2 \tag{6}$$

Using the TM reflection coefficient obtained from Equation (6), the angular reflectance was calculated in Equation (7):

$$R_p = |r_p|^2 \tag{7}$$

where R_p is the reflectance for TM-polarized light and r_p is the TM reflection coefficient obtained from the TMM formulation. The resonance angle, θ_{res}, was defined as the incident angle at which R_p reaches its minimum value. Changes in H_2O_2 concentration in milk were represented by refractive-index variations in the sensing medium, which produce shifts in θ_{res}. All SPR curves were calculated using 5×10^4 angular sampling points to identify the resonance minimum consistently across the evaluated H_2O_2 concentration conditions. To assess the numerical implementation independently from the proposed B-sil/Al/Al_2O_3/WS_2 configuration, the TMM model was also compared with previously published experimental SPR data reported in Ref. [38], using the corresponding optical configuration and material parameters described in that study. The comparison between the calculated and experimental reflectance responses is presented in Supplementary Figure S1.

2.3. Performance Metrics and Optimization Protocol

The sensor performance was evaluated using the resonance-angle shift, angular refractive-index sensitivity, full width at half maximum, detection accuracy, figure of merit, and limit of detection. The angular refractive-index sensitivity was calculated using Equation (8):

$$S_{RI} = \frac{\Delta\theta_{res}}{\Delta n}\left(^\circ\, RIU^{-1}\right) \tag{8}$$

where S_{RI} is the angular refractive-index sensitivity, $\Delta\theta_{res}$ is the resonance-angle shift, and Δn is the refractive-index change of the sensing medium.

The detection accuracy was obtained from the full width at half maximum of the SPR curve using Equation (9):

$$DA = \frac{\Delta\theta}{FWHM}\,(/^\circ) \tag{9}$$

where DA is the detection accuracy and FWHM is the angular full width at half maximum of the resonance dip.

The figure of merit was calculated using Equation (10):

$$FoM = \frac{S_{RI}(1 - R_{min})}{FWHM}\,(\,RIU^{-1}) \tag{10}$$

where R_{min} represents the lowest normalized reflectance value at resonance.

The limit of detection was estimated using Equation (11):

$$LoD = \frac{\Delta n}{\Delta \theta} \times 0.005^{\circ}\ (RIU) \quad (11)$$

where 0.005° is the minimum resolvable angular shift considered in the numerical analysis. The optimization protocol was based on sequential variation of the multilayer structure. The Al layer was optimized first to obtain a well-defined SPR dip with low minimum reflectance. The Al_2O_3 layer was then evaluated as a dielectric and protective coating, followed by the WS_2 layer as the two-dimensional interfacial material. The final configuration was selected by considering high S_{RI}, low *FWHM*, high *DA*, high *FoM*, and low *LoD*. The same numerical conditions were applied to all configurations to allow direct comparison.

3. Results and Discussion

3.1. Prism Selection and Baseline SPR Response

The prism material was evaluated as the first design variable because it controls the optical coupling condition in the Kretschmann configuration. The refractive indices used for the prism-screening stage and the reference media are summarized in Table 2. The tested structures are defined in Table S1. Sys0-BK7 was used as the water-reference structure, while Sys1-BaF_2, Sys2-CaF_2, Sys3-B-sil, and Sys4-BK7 correspond to Al-based SPR configurations in contact with the sensing medium. The sensing medium represents the baseline milk sample before the refractive-index variation associated with H_2O_2 adulteration.

Table 2. Refractive indices of prism materials and reference media used for the SPR configuration at λ = 633 nm.

Material	Refractive Index	Ref.
BaF_2	1.4733	[54]
CaF_2	1.4329	[54]
B-sil	1.4701	[46]
BK7	1.5151	[54]
Water medium (H_2O)	1.3300	[55]
Sensing medium (SM) (baseline)	1.3455	[56]

Figure 1a shows that all prism materials produce a distinguishable SPR dip under angular interrogation at 633 nm. The position of this dip depends on the refractive index of the coupling prism listed in Table 2. The BK7/water reference structure shows the resonance near 64.73°, while replacing water with the sensing medium shifts the resonance to 65.88° for BK7/Al/SM. The other prism materials shift the resonance to higher angles, with values of 69.81° for BaF_2, 74.77° for CaF_2, and 70.15° for B-sil glass, as summarized in Table 3. This trend confirms that the prism refractive index modifies the phase-matching condition between the incident optical wave and the surface plasmon mode.

Table 3. SPR response metrics obtained for the Al-based sensor using different prism materials and the sensing-medium baseline.

Code	SPR Peak Position	Δθ (Deg)	Sensitivity Enhancement (%)	Attenuation (%)	FWHM
$Sys_{1\text{-}BaF2}$	69.81	5.43	8.43	4.93	0.43
$Sys_{2\text{-}CaF2}$	74.77	10.39	16.14	3.90	0.58
$Sys_{3\text{-}B\text{-}sil}$	70.15	5.77	8.97	4.91	0.44
$Sys_{4\text{-}BK7}$	65.88	1.15	2.32	6.14	0.35

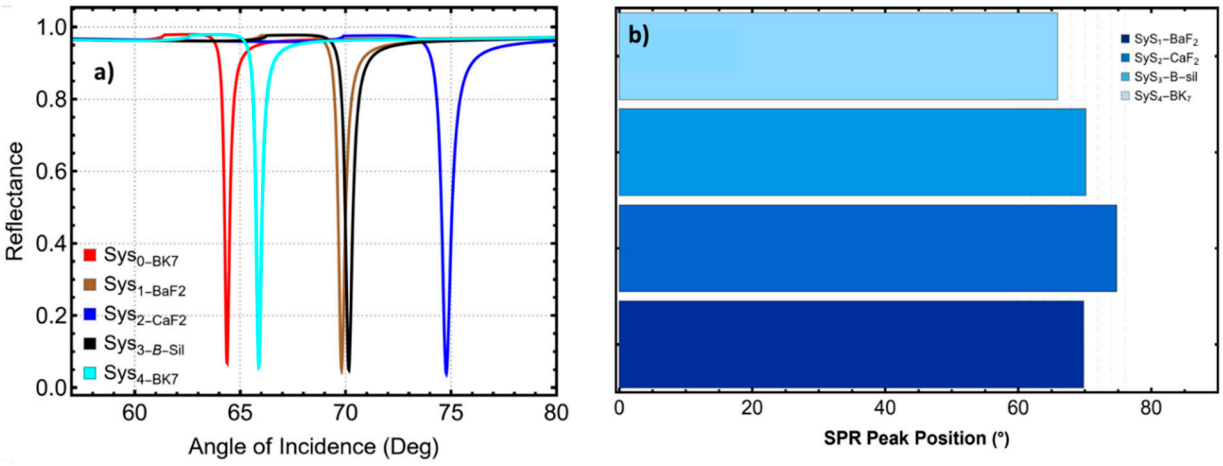


Figure 1. Effect of prism material on the baseline SPR response: (**a**) angular reflectance curves for BK7/Al/H_2O and prism/Al/sensing-medium configurations and (**b**) SPR peak position obtained for BaF_2, CaF_2, B-sil glass, and BK7 substrates.

The resonance-angle shift, ΔθSPR, provides a direct measure of the response generated by changing the external medium from water to the milk baseline. As shown in Figure 2a and Table 3, CaF_2 gives the largest ΔθSPR of 10.39°, followed by B-sil glass with 5.77°, BaF_2 with 5.43°, and BK7 with 1.15°. The same order is observed for sensitivity enhancement, where CaF_2 reaches 16.14%, B-sil glass reaches 8.97%, BaF_2 reaches 8.43%, and BK7 reaches 2.32% (Figure 2b). These results indicate that CaF_2 gives the strongest angular displacement during the prism-screening stage, while B-sil glass provides an intermediate response that remains clearly separated from the BK7-based sensing case.

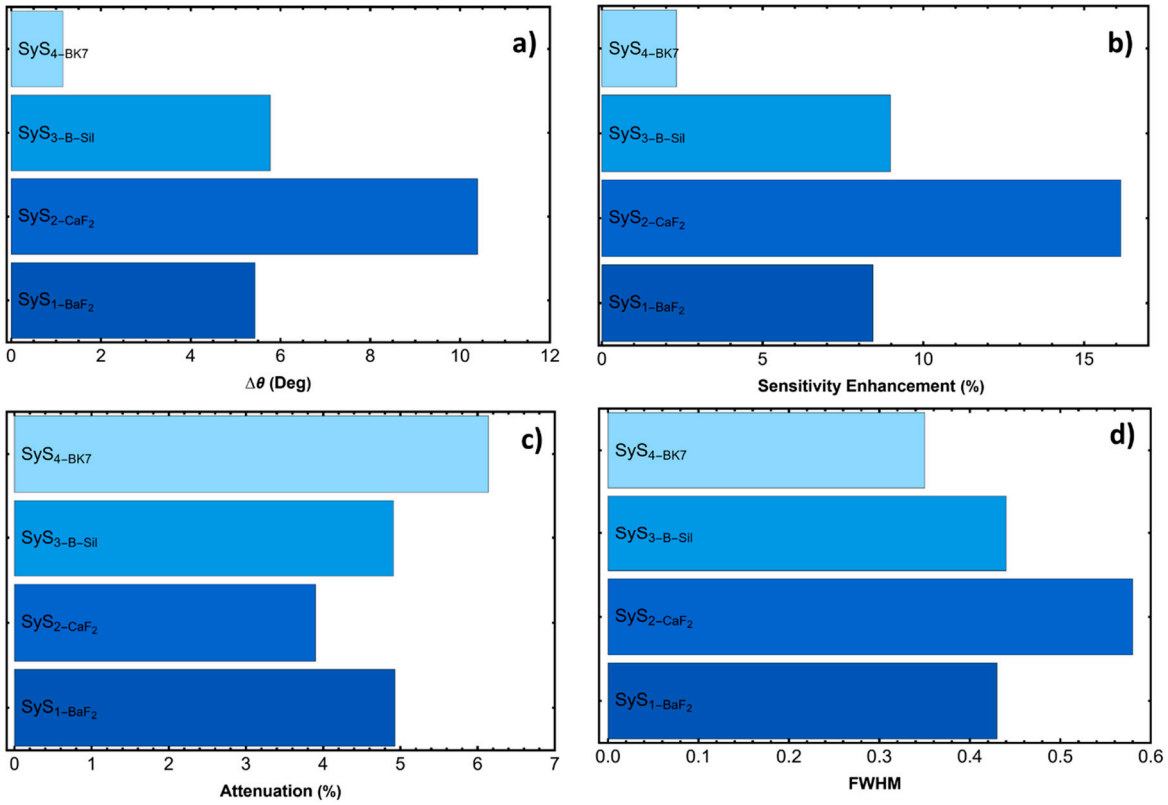


Figure 2. Prism-dependent sensing metrics of the Al-based SPR platform: (**a**) resonance-angle shift, $\Delta\theta_{SPR}$, (**b**) sensitivity enhancement, (**c**) Attenuation, and (**d**) FWHM.

The attenuation and resonance width were also considered because a useful SPR configuration requires both a measurable angular shift and a well-defined resonance profile. The attenuation values range from 3.90% for CaF_2 to 6.14% for BK7, with B-sil glass giving 4.91% (Figure 2c and Table 3). The FWHM values are 0.43° for BaF_2, 0.58° for CaF_2, 0.44° for B-sil glass, and 0.35° for BK7 (Figure 2d). Although BK7 gives the narrowest resonance, its small ΔθSPR limits its usefulness for the present sensing design. CaF_2 gives the largest angular response, but its resonance is broader than those obtained with BaF_2 and B-sil glass. B-sil glass provides a balanced baseline response, combining a moderate angular shift of 5.77°, sensitivity enhancement of 8.97%, attenuation of 4.91%, and FWHM of 0.44°.

Based on these results, B-sil glass was selected as the prism material for the subsequent optimization steps. This selection does not imply that B-sil is universally superior to the other prisms. Rather, it provides a suitable compromise between angular response, resonance definition, and compatibility with the proposed multilayer architecture. The B-sil-supported Al configuration was therefore retained as the baseline structure for the subsequent Al, Al_2O_3, and WS_2 optimization stages.

3.2. Effect of Aluminum Thickness on the SPR Response of the B-Sil/Al Platform

After selecting B-sil glass as the prism material, the thickness of the Al plasmonic layer was varied to define the baseline metal film for the SPR platform. The refractive-index values reported in Table 2 were used for the B-sil prism, water reference medium, and sensing-medium baseline. For the metallic layer, the complex refractive index of Al at λ = 633 nm was taken as 0.0778 + 5.8535i [54]. The tested structures are described in Table S2, while the corresponding optical response metrics are summarized in Table 4. The Al thickness was evaluated at 45, 50, 60, and 70 nm under the same angular interrogation conditions used in the prism-selection step. The sensing medium was kept at the baseline milk refractive index to isolate the effect of the metal-layer thickness on the resonance profile.

Table 4. SPR response metrics obtained for the B-sil/Al/sensing-medium platform at different Al thicknesses.

Code	Thickness (nm)	SPR Peak Position	Δθ (Deg)	Sensitivity Enhancement (%)	Attenuation (%)	FWHM
$Sys_{1\text{-Al-45nm}}$	45	70.15	1.84	2.70	4.91	0.44
$Sys_{2\text{-Al-50nm}}$	50	70.14	1.83	2.67	22.55	0.37
$Sys_{3\text{-Al-60nm}}$	60	70.12	1.81	2.65	63.63	2153.04
$Sys_{4\text{-Al-70nm}}$	70	70.12	1.81	2.65	85.60	38.60

Figure 3a shows that changing the Al thickness modifies both the depth and width of the SPR dip. At 45 nm, the reflectance minimum is well defined and occurs near 70.15°. Increasing the thickness to 50 nm preserves a similar resonance position, with the SPR peak located at 70.14°. For 60 and 70 nm, the resonance position remains close to 70.12°, indicating that the angular location of the SPR minimum is only weakly affected once the Al film exceeds 50 nm. This limited angular displacement is also observed in Figure 3b and Table 4, where Δθ decreases slightly from 1.84° at 45 nm to 1.81° at 60–70 nm.

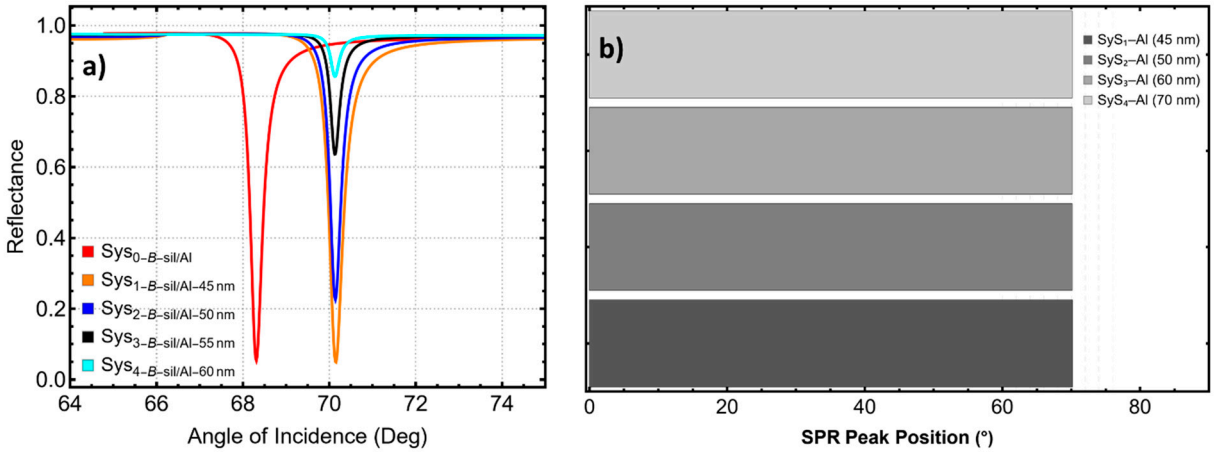


Figure 3. Aluminum-thickness-dependent SPR response of the B-sil-supported Al platform: (**a**) angular reflectance profiles for 45, 50, 60, and 70 nm Al layers and (**b**) corresponding SPR peak positions.

The sensitivity enhancement follows the same modest trend. As shown in Figure 4b, the enhancement decreases from 2.70% for the 45 nm Al layer to 2.65% for the 60 and 70 nm cases. This small variation indicates that the angular response alone is not sufficient to select the Al thickness. The attenuation and FWHM must also be considered because they describe the strength and definition of the resonance dip. Table 4 shows that attenuation increases from 4.91% at 45 nm to 22.55% at 50 nm, 63.63% at 60 nm, and 85.60% at 70 nm. This trend is also shown in Figure 4c and reflects stronger damping of the reflected signal as the Al layer becomes thicker.

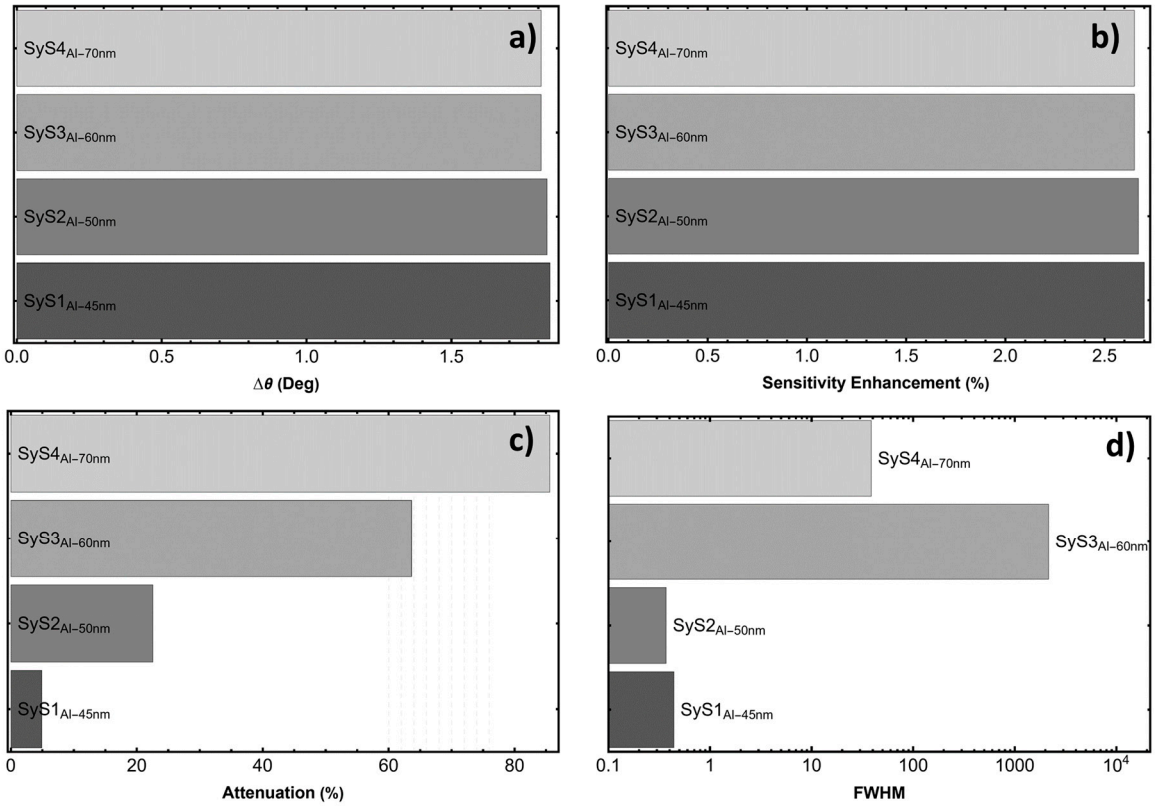


Figure 4. Aluminum-thickness-dependent sensing metrics of the B-sil-supported Al platform: (**a**) resonance-angle shift, $\Delta\theta_{SPR}$, (**b**) sensitivity enhancement, (**c**) attenuation, and (**d**) FWHM.

The FWHM response is less uniform. The 45 and 50 nm films give narrow resonance profiles, with FWHM values of 0.44° and 0.37°, respectively. At 60 nm, the FWHM increases to 2153.04°, which indicates a poorly defined resonance profile under the numerical conditions used. The 70 nm film gives a lower FWHM than the 60 nm case but remains broader than the 45 and 50 nm films, with a value of 38.60°. This broadening suggests that thicker Al films reduce the sharpness of the angular resonance, even though they increase attenuation.

The 70 nm Al layer was retained for the next stage of the multilayer design. This choice was not defined by a single performance parameter. The 45 and 50 nm films produced sharper resonance dips, whereas the 70 nm film provided the strongest attenuation and maintained a stable SPR peak position near 70.12°. The next design step introduces an Al_2O_3 dielectric coating and a WS_2 interfacial layer; for that reason, the 70 nm Al film was used as the baseline metal layer to evaluate how the added layers reshape the resonance profile and modify the sensor response. This choice should be interpreted as a design condition for the proposed multilayer sequence rather than as a general optimum for all Al-based SPR sensors.

3.3. Al_2O_3 Thickness Selection in the B-Sil/Al SPR Platform

The Al_2O_3 coating was introduced after fixing the B-sil/Al platform to examine how a dielectric overlayer modifies the plasmonic response. The structures used in this stage are defined in Table S3. The optical parameters are given in Table S4; the B-sil, water, and sensing-medium refractive indices follow the values reported in Table 2, the Al layer was fixed at 70 nm using a complex refractive index of 0.0778 + 5.8535i [54], and Al_2O_3 was modeled with a refractive index of 1.77 [57]. The coating thickness was varied from 2 to 30 nm while keeping the sensing medium at its baseline refractive index.

The reflectance curves in Figure 5a show a progressive displacement of the resonance dip as the Al_2O_3 layer becomes thicker. With a 2 nm coating, the resonance appears at 70.60°, which remains close to the response of the uncoated Al platform. At 15 nm, the dip shifts to 74.95°. A further increase to 25 nm moves the resonance to 80.94°, while the 30 nm coating places the resonance at 87.38° (Figure 5b and Table 5). This trend indicates that the Al_2O_3 layer is not acting only as a passive protective film; it changes the optical phase condition of the multilayer and moves the SPR mode toward higher incidence angles.

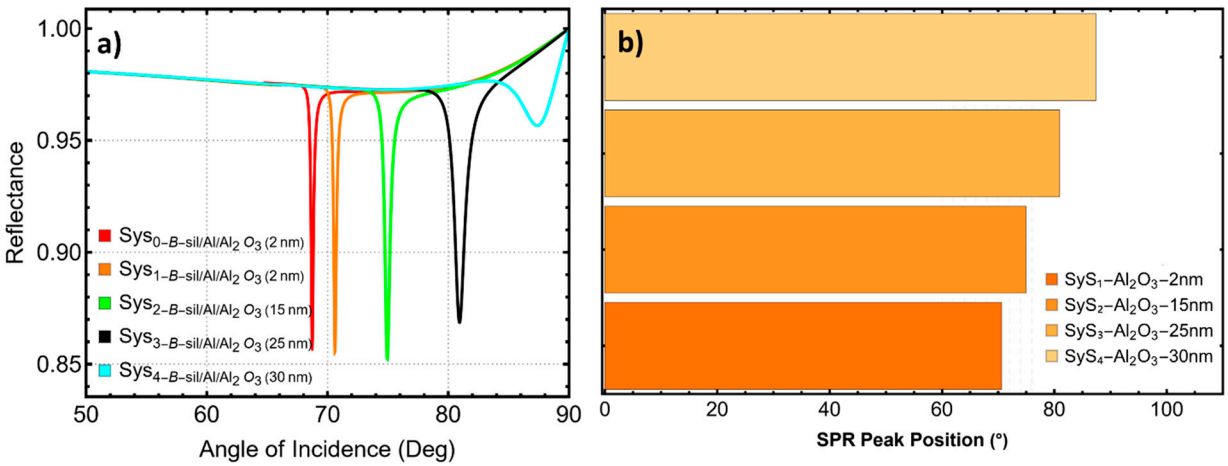


Figure 5. Al_2O_3-thickness-dependent SPR response of the B-sil/Al/Al_2O_3 platform: (**a**) angular reflectance profiles for 2, 15, 25, and 30 nm Al_2O_3 layers and (**b**) corresponding SPR peak positions.

Table 5. SPR response metrics obtained for the B-sil/Al/Al_2O_3/sensing-medium platform at different Al_2O_3 thicknesses.

Code	Thickness (nm)	SPR Peak Position	Δθ (Deg)	Sensitivity Enhancement (%)	Attenuation (%)	FWHM
$Sys_{1\text{-Al+Al2O3-2nm}}$	2	70.60	1.87	2.72	85.54	38.11
$Sys_{2\text{-Al+Al2O3-15nm}}$	15	74.95	6.22	9.05	85.22	36.44
$Sys_{3\text{-Al+Al2O3-25nm}}$	25	80.94	12.21	17.76	86.86	46.84
$Sys_{4\text{-Al+Al2O3-30nm}}$	30	87.38	18.64	27.12	95.66	99.01

The increase in $\Delta\theta_{SPR}$ follows this angular displacement. Table 5 reports $\Delta\theta_{SPR}$ values of 1.87°, 6.22°, 12.21°, and 18.64° for Al_2O_3 thicknesses of 2, 15, 25, and 30 nm, respectively. The sensitivity enhancement also increases across the same thickness range, from 2.72% to 27.12%, as shown in Figure 6a,b. This behavior is consistent with a stronger contribution of the dielectric layer to the evanescent-field distribution near the sensing interface. In practical terms, the thicker coatings give a larger angular displacement, but this gain must be interpreted together with the resonance profile.

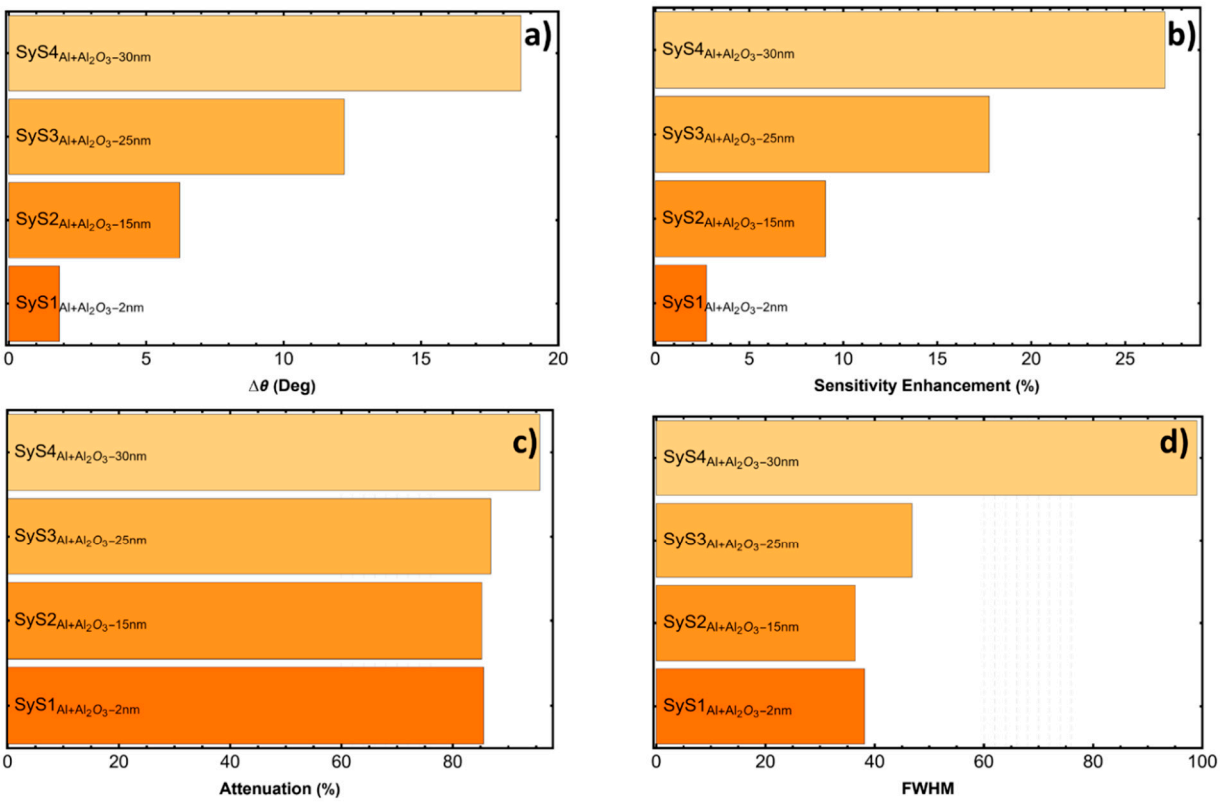


Figure 6. Al_2O_3-thickness-dependent sensing metrics of the B-sil/Al/Al_2O_3 platform: (**a**) resonance-angle shift, $\Delta\theta_{SPR}$, (**b**) sensitivity enhancement, (**c**) attenuation, and (**d**) FWHM.

The attenuation values remain within a relatively high range for the four Al_2O_3-coated structures. The 2, 15, and 25 nm layers give attenuation values of 85.54%, 85.22%, and 86.86%, respectively, while the 30 nm layer increases attenuation to 95.66% (Figure 6c and Table 5). The FWHM response shows the trade-off more clearly. The 15 nm coating gives the lowest FWHM among the tested Al_2O_3 cases, with 36.44°, followed by 2 nm with 38.11° and 25 nm with 46.84°. At 30 nm, the FWHM increases to 99.01° (Figure 6d), indicating that

the resonance becomes much broader when the dielectric layer is too thick for the selected angular range.

The 25 nm Al_2O_3 layer was selected for the next stage because it gives a workable compromise between angular displacement and resonance definition. Compared with 2 and 15 nm, the 25 nm coating provides a larger $\Delta\theta_{SPR}$ and sensitivity enhancement. Compared with 30 nm, it avoids shifting the resonance too close to the high-angle edge of the scan and keeps the FWHM markedly lower. This condition gave $\Delta\theta_{SPR}$ = 12.21°, sensitivity enhancement = 17.76%, attenuation = 86.86%, and FWHM = 46.84° (Table 5). The B-sil/Al/Al_2O_3 platform with 70 nm Al and 25 nm Al_2O_3 was therefore used for the subsequent evaluation of the WS_2 interfacial layer.

3.4. Selection of the WS_2 Interfacial Layer in the B-Sil/Al/Al_2O_3 SPR Platform

The final material-selection step examined the effect of adding a 2D interfacial layer to the B-sil/Al/Al_2O_3 platform. The evaluated structures are defined in Table S5, and the optical constants and layer thicknesses used in the simulation are reported in Table S6. The platform retained the previously selected B-sil prism, 70 nm Al layer, and 25 nm Al_2O_3 coating. The tested 2D materials were black phosphorus (BP), molybdenum disulfide (MoS_2), molybdenum diselenide ($MoSe_2$), and tungsten disulfide (WS_2), using refractive indices of 3.50 + 0.01i, 5.0805 + 1.1723i, 4.62 + 1.0063i, and 4.90 + 0.3124i, respectively, at λ = 633 nm (Table S6) [54]. Water and the sensing-medium baseline were kept at the refractive-index values used in the previous stages.

Figure 7a shows that the 2D layer changes the depth and angular position of the resonance dip. The BP-coated system gives the resonance at 78.64°, close to the reference condition of the coated platform. The TMDC-containing structures shift the resonance toward higher angles, with peak positions of 79.95° for MoS_2, 79.80° for $MoSe_2$, and 80.59° for WS_2 (Figure 7b and Table 6). This displacement indicates that the interfacial material contributes to the phase condition of the multilayer and alters the optical interaction at the sensing boundary.

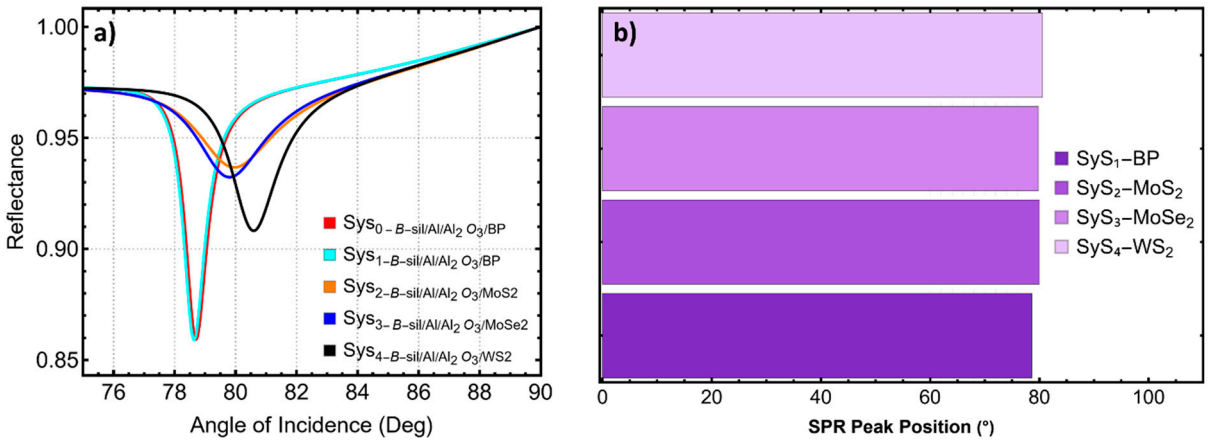


Figure 7. Effect of the 2D interfacial material on the angular SPR response of the B-sil/Al/Al_2O_3 platform: (**a**) reflectance curves for BP, MoS_2, $MoSe_2$, and WS_2 interfacial layers and (**b**) corresponding SPR peak positions.

The angular-shift data in Table 6 show that BP produces a small $\Delta\theta_{SPR}$ of 0.06°, whereas MoS_2 and $MoSe_2$ produce larger shifts of 1.24° and 1.09°, respectively. WS_2 gives the highest value among the tested 2D layers, with $\Delta\theta_{SPR}$ = 1.89°. The same tendency is observed for sensitivity enhancement in Figure 8b, where WS_2 reaches 2.40%, followed by MoS_2 at 1.58%, $MoSe_2$ at 1.39%, and BP at 0.07%. These differences are consistent with the

distinct optical constants of the 2D layers, which modify the evanescent-field interaction near the analyte interface.

Table 6. SPR response metrics of the B-sil/Al/Al_2O_3/sensing-medium platform after incorporating different 2D interfacial materials.

Code	SPR Peak Position	Δθ (Deg)	Sensitivity Enhancement (%)	Attenuation (%)	FWHM
$Sys_{1\text{-B-sil/Al/Al2O3/BP/SM}}$	78.64	0.06	0.07	85.91	38.82
$Sys_{2\text{-B-sil/Al/Al2O3/MoS2/SM}}$	79.95	1.24	1.58	93.66	44.72
$Sys_{3\text{-B-sil/Al/Al2O3/MoSe2/SM}}$	79.80	1.09	1.39	93.22	43.89
$Sys_{4\text{-B-sil/Al/Al2O3/WS2/SM}}$	80.59	1.89	2.40	90.81	44.84

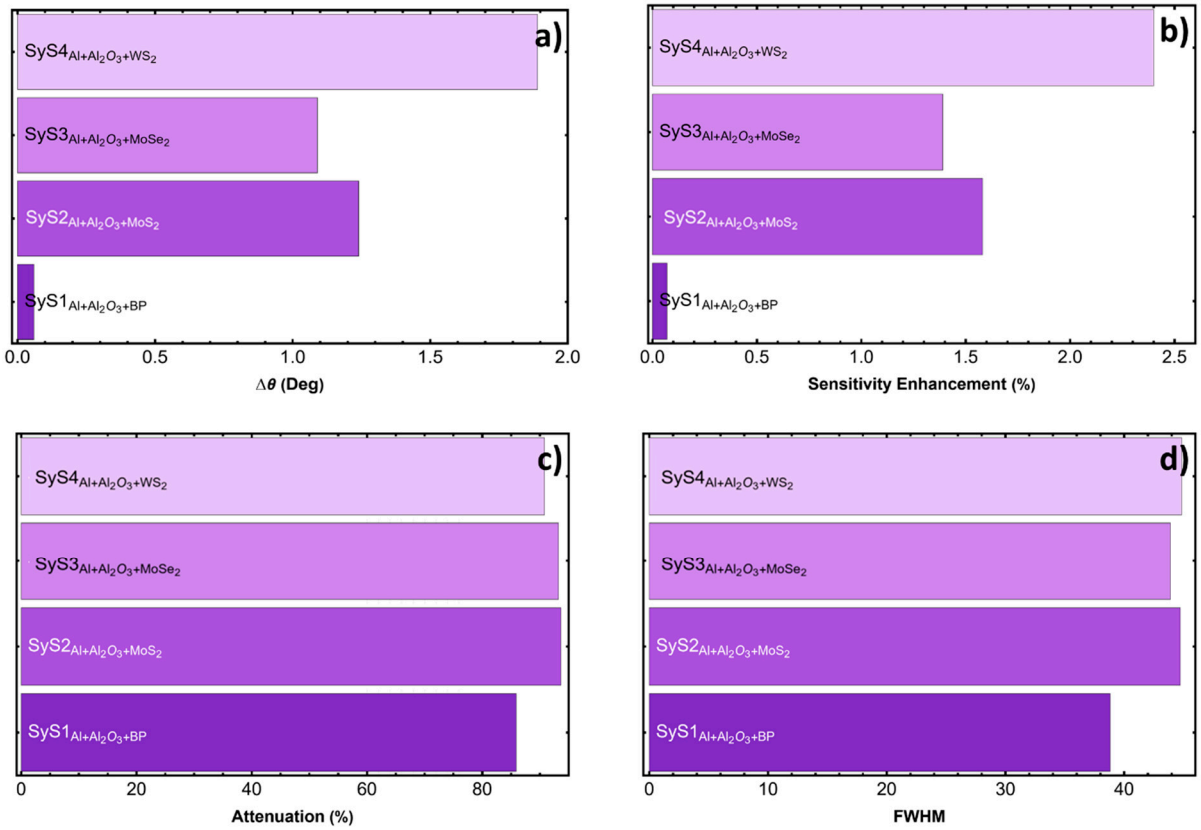


Figure 8. Effect of the 2D interfacial material on the sensing metrics of the B-sil/Al/Al_2O_3 platform: (**a**) resonance-angle shift, $\Delta\theta_{SPR}$, (**b**) sensitivity enhancement, (**c**) attenuation, and (**d**) FWHM.

Attenuation remains high for the four interfacial materials, as shown in Figure 8c. Table 6 reports attenuation values of 85.91% for BP, 93.66% for MoS_2, 93.22% for $MoSe_2$, and 90.81% for WS_2. MoS_2 and $MoSe_2$ give slightly higher attenuation than WS_2, but their angular shifts and sensitivity enhancements are lower. The FWHM values also remain within a comparable range for the TMDC-based structures. BP gives the lowest FWHM, 38.82°, while MoS_2, $MoSe_2$, and WS_2 give 44.72°, 43.89°, and 44.84°, respectively (Figure 8d and Table 6). The WS_2 case therefore introduces only a modest broadening relative to the other TMDCs while giving the largest angular response.

WS_2 was selected as the interfacial layer for the final sensing configuration. This selection reflects the balance between angular displacement, sensitivity enhancement, attenuation, and resonance width rather than a single isolated metric. At the selected

condition, the B-sil/Al/Al_2O_3/WS_2/sensing-medium structure produced an SPR peak at 80.59°, $\Delta\theta_{SPR}$ = 1.89°, sensitivity enhancement = 2.40%, attenuation = 90.81%, and FWHM = 44.84° (Table 6). These values indicate that WS_2 provides a suitable interfacial condition for the following H_2O_2-dependent refractive-index analysis while preserving a measurable resonance profile within the simulated angular range.

3.5. B-Sil/Al/Al_2O_3/WS_2 Sensor Under Different H_2O_2 Concentration Levels in Milk

The response of the selected B-sil/Al/Al_2O_3/WS_2 structure was examined using milk media containing increasing H_2O_2 concentrations. The simulated conditions comprised the baseline sensing medium, denoted SM, and six H_2O_2-containing samples, denoted C1–C6. The concentration and refractive-index values assigned to each condition are reported in Table 7. H_2O_2 concentration increased from 0.00% for SM to 14.29% for C6, while the refractive index increased from 1.34550 to 1.34686. The multilayer configuration consisted of a B-sil prism, a 70 nm Al layer, a 25 nm Al_2O_3 coating, and a 0.80 nm WS_2 interfacial layer. Angular interrogation was performed at λ = 633 nm.

Table 7. Concentration vs Refractive index.

Code	Concentration (%)	RI
SM	0.0000	1.34550
C1	1.63934	1.34566
C2	3.22581	1.34581
C3	6.25000	1.34609
C4	9.09091	1.34636
C5	11.76471	1.34662
C6	14.28571	1.34686

Figure 9a shows that the reflectance profiles retain a similar shape across the simulated concentration range, while the resonance minimum shifts toward higher incidence angles as the H_2O_2 concentration and refractive index increase. The corresponding peak positions are shown in Figure 9b and summarized in Table 8. The resonance angle changes from 85.65° for C1 to 86.11° for C6, giving a total displacement of 0.46° between the lowest and highest simulated H_2O_2 conditions.

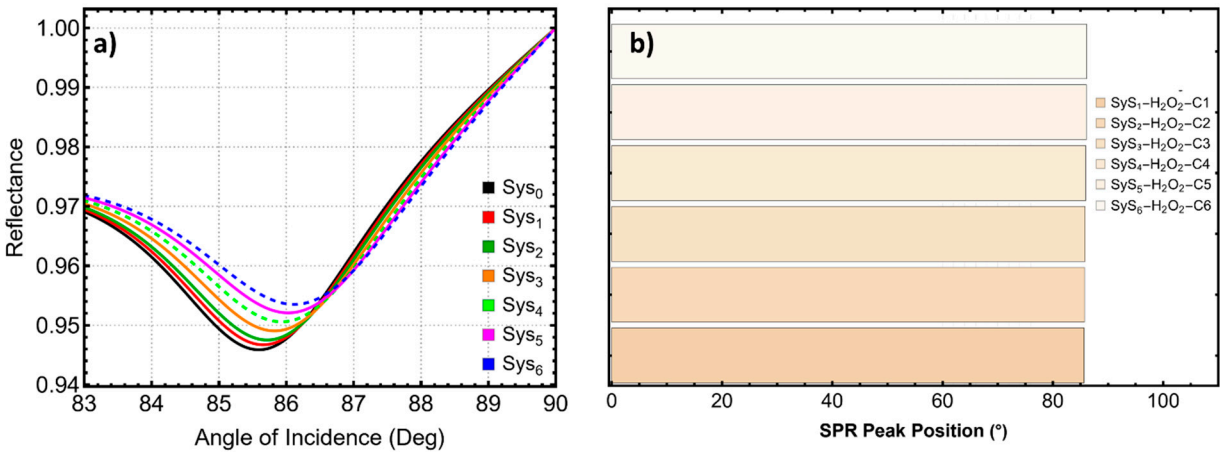


Figure 9. H_2O_2-dependent angular SPR response of the optimized B-sil/Al/Al_2O_3/WS_2 sensor: (**a**) reflectance profiles for the baseline and H_2O_2-containing milk media and (**b**) SPR peak positions.

Table 8. SPR response metrics of the optimized B-sil/Al/Al_2O_3/WS_2 sensor for the simulated H_2O_2 concentration levels in milk.

Code	SPR Peak Position	Δθ (Deg)	Sensitivity Enhancement (%)	Attenuation (%)	FWHM
Sys_{1}-B-sil/Al/Al2O3/WS2/H2O2-C1	85.65	0.06	0.073	94.67	86.80
Sys_{2}-B-sil/Al/Al2O3/WS2/H2O2-C2	85.71	0.12	0.147	94.75	87.30
Sys_{3}-B-sil/Al/Al2O3/WS2/H2O2-C3	85.82	0.23	0.273	94.90	88.03
Sys_{4}-B-sil/Al/Al2O3/WS2/H2O2-C4	85.93	0.34	0.399	95.05	88.45
Sys_{5}-B-sil/Al/Al2O3/WS2/H2O2-C5	86.03	0.44	0.515	95.20	88.53
Sys_{6}-B-sil/Al/Al2O3/WS2/H2O2-C6	86.11	0.52	0.609	95.35	88.30

The resonance-angle shift was calculated relative to the baseline sensing medium. As reported in Table 8 and shown in Figure 10a, $\Delta\theta_{SPR}$ increases from 0.06° for C1 to 0.52° for C6. This monotonic response follows the refractive-index increase listed in Table 7, from 1.34566 for C1 to 1.34686 for C6. The sensitivity enhancement follows the same trend, increasing from 0.073% to 0.609%, as shown in Figure 10b and Table 8.

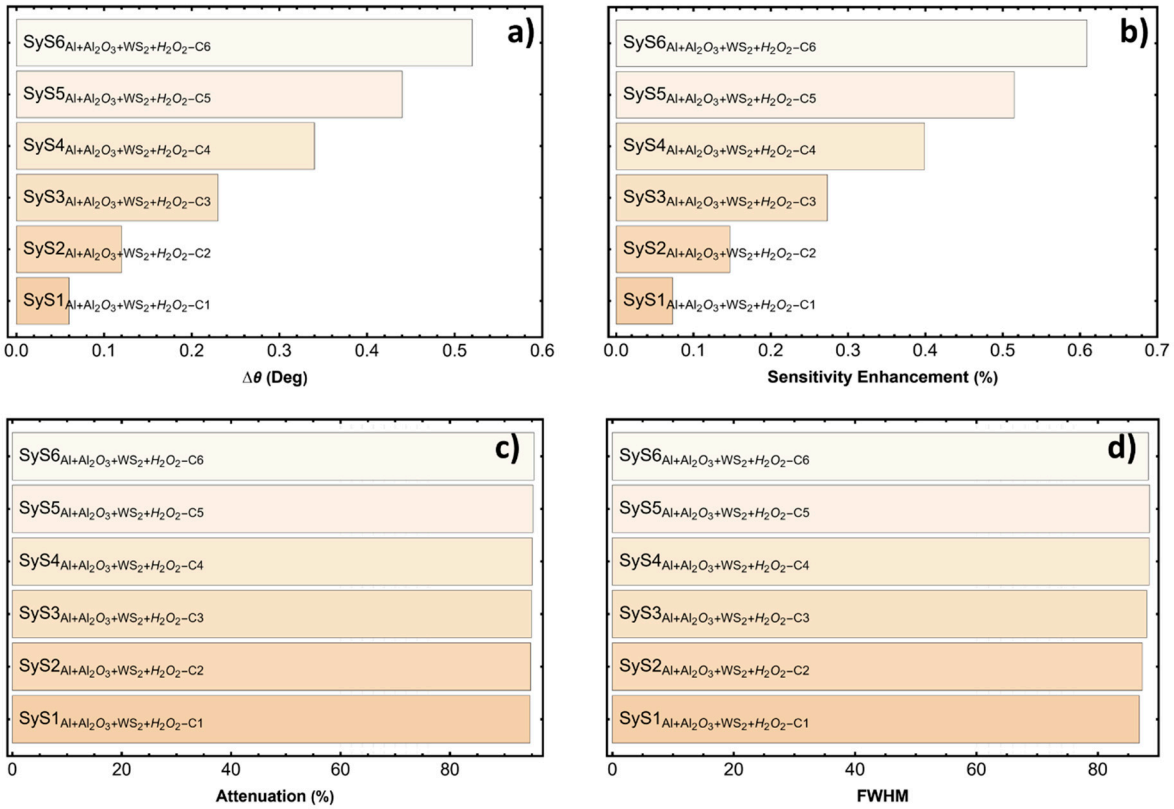


Figure 10. H_2O_2-dependent response metrics of the optimized B-sil/Al/Al_2O_3/WS_2 sensor: (**a**) resonance-angle shift, $\Delta\theta_{SPR}$, (**b**) sensitivity enhancement, (**c**) attenuation, and (**d**) FWHM.

The calculated response is governed by bulk refractive-index variation rather than selective chemical recognition of H_2O_2. The model therefore represents an optical screening approach in which changes in milk composition modify the phase-matching condition of the SPR mode. Experimental measurements would be required to determine whether the angular shift can be distinguished from refractive-index changes caused by other milk constituents or adulterants.

The attenuation changes only slightly across the concentration series, ranging from 94.67% to 95.35%, as reported in Table 8 and shown in Figure 10c. This limited variation indicates that increasing H_2O_2 concentration affects the angular position of the resonance more strongly than its minimum reflectance. The FWHM values range from 86.80° to 88.53° (Table 8 and Figure 10d), indicating a broad resonance profile under the present numerical conditions. These width values should be verified from the two half-depth crossing angles before FWHM-dependent performance metrics are interpreted.

The selected B-sil/Al/Al_2O_3/WS_2 structure therefore produces a monotonic angular response to the simulated H_2O_2-induced refractive-index variation. Across C1–C6, the resonance angle and $\Delta\theta_{SPR}$ increase with H_2O_2 concentration, while attenuation remains within a narrow interval. These angular shifts provide the basis for calculating refractive-index sensitivity after the FWHM extraction and the associated width-dependent metrics have been verified.

3.6. H_2O_2 Concentration-Dependent Sensing Performance of the Optimized B-Sil/Al/Al_2O_3/WS_2 Sensor

The concentration-dependent performance of the selected B-sil/Al/Al_2O_3/WS_2 configuration was evaluated from the angular shifts calculated for six modeled H_2O_2 cases in milk. The corresponding metrics are reported in Table 9 and Figure 11. This analysis extends the angular response discussed in Section 3.5 by expressing the resonance shifts in terms of angular sensitivity, detection accuracy, quality factor, figure of merit, estimated limit of detection, and combined sensitivity factor.

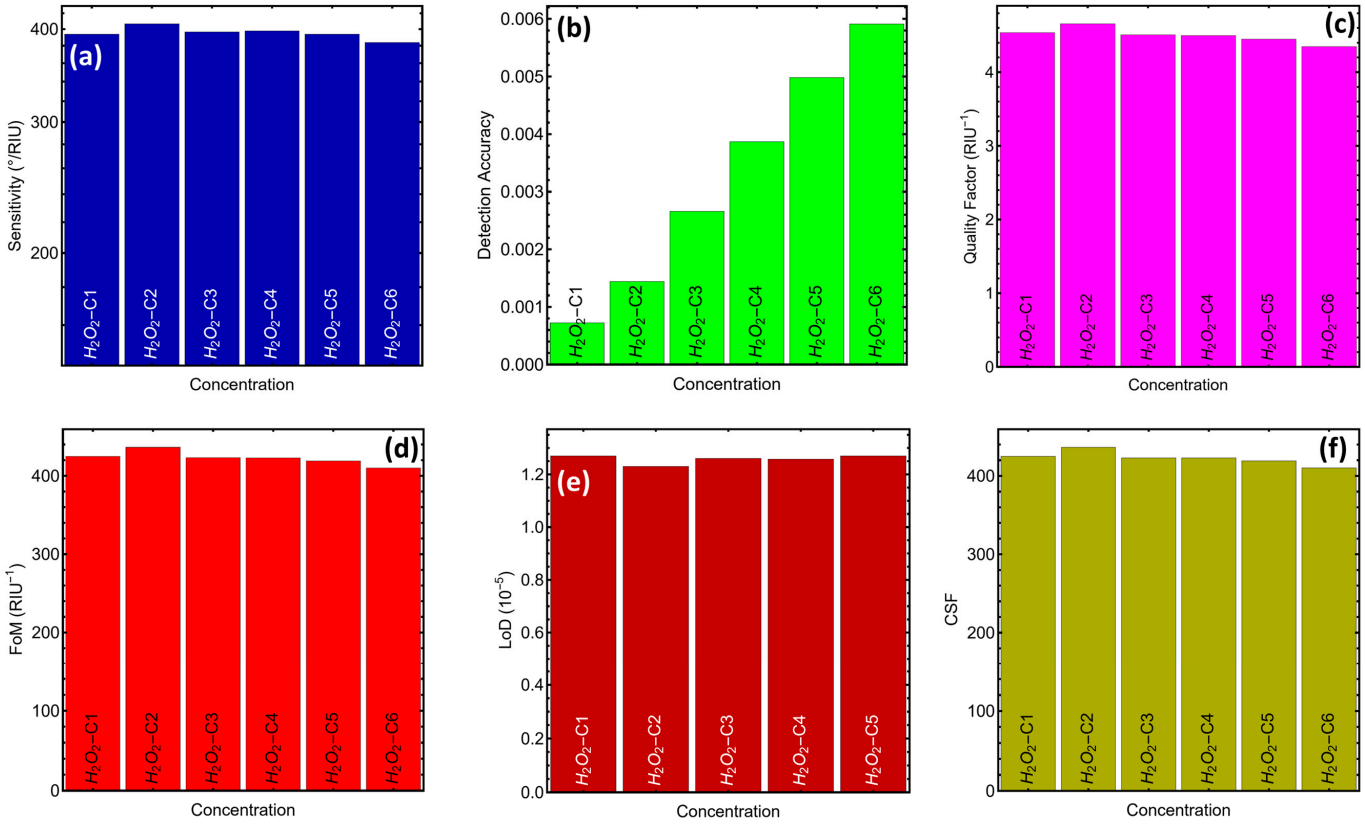


Figure 11. Concentration-dependent performance of the selected B-sil/Al/Al_2O_3/WS_2 SPR configuration under H_2O_2-associated refractive-index variations in milk: (**a**) angular sensitivity, (**b**) detection accuracy, (**c**) quality factor, (**d**) figure of merit, (**e**) estimated limit of detection, and (**f**) combined sensitivity factor.

Table 9. Concentration-dependent performance metrics of the selected B-sil/Al/Al_2O_3/WS_2 SPR configuration under H_2O_2-associated refractive-index variations in milk.

Concentration	*S* (°/*RIU*)	DA	QF (RIU^{-1})	FoM (RIU^{-1})	LoD (10^{-5})	CSF
H_2O_2-C1	393.75	0.00072	4.53	424.88	1.269	424.96
H_2O_2-C2	406.45	0.00144	4.65	436.48	1.230	436.56
H_2O_2-C3	396.61	0.00265	4.50	423.07	1.260	423.15
H_2O_2-C4	397.67	0.00386	4.49	422.88	1.257	422.96
H_2O_2-C5	393.75	0.00498	4.44	418.97	1.269	419.05
H_2O_2-C6	383.82	0.00591	4.34	410.10	1.302	410.18

The angular sensitivity remains within a narrow range, from 383.82 to 406.45°/RIU (Table 9). Figure 11a shows that H_2O_2-C2 gives the highest sensitivity, while lower values are obtained for the remaining cases. This variation indicates that the calculated angular response is not strictly linear over the full simulated refractive-index range. The lower sensitivity values at higher H_2O_2 levels can be associated with the smaller incremental resonance displacement relative to the refractive-index change used in the sensitivity calculation. Despite this variation, all six cases remain within the same order of magnitude, indicating a comparable angular response over the evaluated refractive-index range.

Detection accuracy shows a different pattern. As shown in Figure 11b, DA increases from 0.00072 for H_2O_2-C1 to 0.00591 for H_2O_2-C6. This behavior is linked to the FWHM-dependent definition of DA used in the calculations. The higher DA values obtained for the later H_2O_2 cases reflect the corresponding resonance widths. These values must therefore be interpreted together with the FWHM results reported in the previous section, since DA is derived directly from the calculated resonance width rather than from an independently measured experimental resolution.

The quality factor and figure of merit show a similar distribution. The QF reaches its highest value at H_2O_2-C2, with 4.65 RIU^{-1}, and subsequently decreases to 4.34 RIU^{-1} at H_2O_2-C6 (Figure 11c and Table 9). The FoM also reaches its maximum at H_2O_2-C2, with 436.48 RIU^{-1}, and decreases to 410.10 RIU^{-1} at H_2O_2-C6 (Figure 11d). The combined sensitivity factor follows the same pattern, with a maximum of 436.56 at H_2O_2-C2 and a minimum of 410.18 at H_2O_2-C6 (Figure 11f). Within the present numerical dataset, H_2O_2-C2 gives the largest calculated values of sensitivity, QF, FoM, and CSF.

The estimated limit of detection varies only slightly, ranging from 1.230×10^{-5} to 1.302×10^{-5} (Table 9). Figure 11e shows the lowest estimated LoD at H_2O_2-C2, with higher values for the other evaluated cases. This limited variation reflects the relatively narrow range of calculated angular sensitivity. The minimum estimated LoD therefore occurs at the same H_2O_2 case that gives the largest sensitivity, QF, FoM, and CSF.

Taken together, Table 9 and Figure 11 characterize the optical response of the selected B-sil/Al/Al_2O_3/WS_2 configuration for the six H_2O_2-associated refractive-index cases evaluated in milk. H_2O_2-C2 gives the largest calculated sensitivity, QF, FoM, and CSF and the lowest estimated LoD within the modeled dataset. At higher H_2O_2 levels, DA is larger while the sensitivity-related metrics are lower. These results describe the numerical response of the multilayer structure at the evaluated points and should not be interpreted as evidence of chemical selectivity toward H_2O_2. Further numerical refinement should focus on the resonance profile and its influence on FWHM-dependent metrics before experimental implementation is considered.

3.7. Electric Field Distribution Analysis

The electric-field profile was examined to identify how the optical field is distributed across the optimized multilayer structure and how it extends into the H_2O_2-containing sensing medium. Figure 12a shows the normalized electric-field distribution from the Al layer to the analyte region. The field remains low inside the Al film, increases near the Al/Al_2O_3 region, and reaches its maximum close to the WS_2/analyte interface. This localization is consistent with SPR excitation, where the evanescent field is concentrated near the metal–dielectric boundary and decays into the external medium.

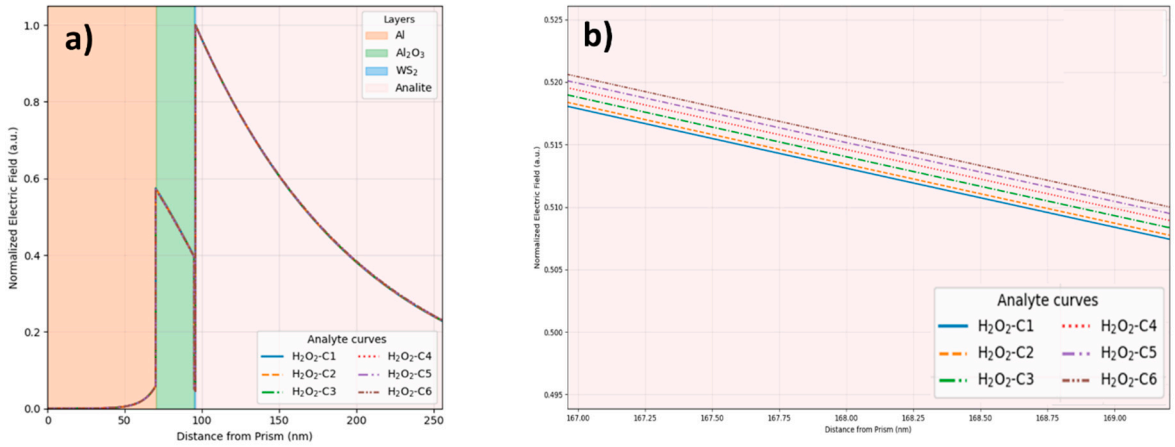


Figure 12. Normalized electric-field distribution of the optimized B-sil/Al/Al_2O_3/WS_2 SPR sensor for H_2O_2 detection in milk: (**a**) field profile across the multilayer stack and analyte region and (**b**) magnified field decay within the sensing medium for the modeled H_2O_2 concentration levels.

The selected structure contains three functional regions before the analyte: Al as the plasmonic layer, Al_2O_3 as the dielectric coating, and WS_2 as the interfacial layer. In Figure 12a, the field increases through the dielectric region and changes sharply near the WS_2/analyte boundary. This behavior indicates that the sensing response is governed by the optical field present at the outer interface, where the milk/H_2O_2 medium is located. Because the evanescent field penetrates into the analyte region, changes in the refractive index of the milk medium can modify the resonance condition and produce the angular shifts discussed in Sections 3.5 and 3.6.

Figure 12b presents a magnified view of the field decay inside the analyte region. The curves associated with H_2O_2-C1 to H_2O_2-C6 show similar decay profiles, with small separation among concentration levels. This result is expected because the modeled H_2O_2 concentrations introduce relatively small refractive-index changes in the sensing medium. The field amplitude decreases with distance from the WS_2/analyte interface, confirming that the strongest optical interaction occurs near the sensor surface. This near-interface sensitivity supports the use of WS_2 as the terminal layer in the proposed configuration.

The field distribution also helps explain the moderate concentration-dependent changes reported in Tables 7 and 8. The resonance angle shifts systematically with H_2O_2 concentration, but the field profiles remain close to each other because the refractive-index contrast between adjacent concentration levels is small. The sensor therefore responds mainly through angular displacement rather than through a large change in field amplitude. This behavior is appropriate for a theoretical refractive-index SPR sensor and indicates that future experimental work should control the analyte–surface contact region carefully, since the sensing signal is concentrated near the WS_2/milk interface.

3.8. Comparison with Reported SPR Studies

The performance of the B-sil/Al/Al_2O_3/WS_2 configuration was compared with reported SPR systems applied to milk adulteration, preservative detection, or milk-composition analysis, as summarized in Table 10. The comparison includes CaF_2/Cu/$BaTiO_3$/graphene for preservative detection in milk [31], ZnSe/Au/graphene/BlueP-MoS_2 for milk adulteration analysis [58], CaF_2/Ag/BP for milk adulteration detection [59], and Ag/barium gallium sulfide/cadmium gallium sulfide/BlueP-MoS_2 for fat-concentration analysis in milk [60]. These studies provide an application-relevant benchmark because they use SPR transduction in milk-related sensing and report at least one of the performance metrics considered in the present work.

Table 10. Comparison of reported SPR-based sensors for milk adulteration detection and the proposed B-sil/Al/Al_2O_3/WS_2 sensor under the simulated H_2O_2 concentration conditions.

Ref.	SPR Structure	Sensitivity (°/RIU)	QF (RIU^{-1})	DA
[31]	CaF_2/Cu/$BaTiO_3$/graphene/SM	219	102.34	0.47
[58]	ZnSe/Au/graphene/BlueP-MoS_2/SM	51.38	No reported	No reported
[59]	CaF_2/Ag/BP/SM	574	200	0.223
[60]	Ag/Barium gallium sulfide/Cadmium gallium sulfide/BlueP-MoS_2/SM	433.02	310.12	No reported
This study	B-sil/Al/Al_2O_3/WS_2/H_2O_2-C1	393.75	4.53	0.00072
This study	B-sil/Al/Al_2O_3/WS_2/H_2O_2-C2	406.45	4.65	0.00144
This study	B-sil/Al/Al_2O_3/WS_2/H_2O_2-C3	396.61	4.50	0.00265
This study	B-sil/Al/Al_2O_3/WS_2/H_2O_2-C4	397.67	4.49	0.00386
This study	B-sil/Al/Al_2O_3/WS_2/H_2O_2-C5	393.75	4.44	0.00498
This study	B-sil/Al/Al_2O_3/WS_2/H_2O_2-C6	383.82	4.34	0.00591

The calculated angular sensitivity of the present configuration ranges from 383.82 to 406.45°/RIU across the six simulated H_2O_2 conditions. This range exceeds the 219°/RIU reported for the CaF_2/Cu/$BaTiO_3$/graphene structure [31] and the 51.38°/RIU reported for the ZnSe/Au/graphene/BlueP-MoS_2 structure [58]. It is also close to the 433.02°/RIU reported for the Ag/barium gallium sulfide/cadmium gallium sulfide/BlueP-MoS_2 platform [60]. The CaF_2/Ag/BP structure shows the highest sensitivity in this comparison, reaching 574°/RIU [59]. The present configuration therefore does not maximize angular sensitivity among the reported systems, but it maintains values above 380°/RIU using an Al-based plasmonic layer combined with Al_2O_3 and WS_2.

The quality factor of the present configuration ranges from 4.34 to 4.65 RIU^{-1}. These values are lower than those reported for CaF_2/Cu/$BaTiO_3$/graphene, CaF_2/Ag/BP, and Ag/barium gallium sulfide/cadmium gallium sulfide/BlueP-MoS_2, which show QF values of 102.34, 200, and 310.12 RIU^{-1}, respectively [31,59,60]. This difference is associated with the broad resonance profiles obtained for the Al/Al_2O_3/WS_2 multilayer. The QF comparison therefore indicates that resonance-width reduction remains an important aspect for further refinement of the configuration.

Detection accuracy increases from 0.00072 to 0.00591 across the simulated H_2O_2 conditions. These values are lower than the DA values of 0.47 and 0.223 reported for the CaF_2/Cu/$BaTiO_3$/graphene and CaF_2/Ag/BP structures, respectively [31,59]. The ZnSe/Au/graphene/BlueP-MoS_2 and Ag/barium gallium sulfide/cadmium gallium sulfide/BlueP-MoS_2 studies did not report DA values [58,60]. This behavior is consis-

tent with the FWHM dependence discussed in Section 3.6 and indicates that the present configuration is more favorable in angular sensitivity than in resonance sharpness.

Among the six simulated conditions, H_2O_2-C2 gives the largest calculated sensitivity and QF, with values of 406.45°/RIU and 4.65 RIU^{-1}, respectively, while its DA is 0.00144. H_2O_2-C6 gives the highest DA but the lowest sensitivity and QF within the modeled series. Within this numerical comparison, the B-sil/Al/Al_2O_3/WS_2 configuration can be interpreted as a sensitivity-oriented theoretical SPR architecture for evaluating H_2O_2-associated refractive-index variations in milk. Further work should focus on narrowing the resonance profile, experimentally validating the H_2O_2-associated refractive-index response in real milk samples, and incorporating an appropriate selective recognition or filtering strategy for practical implementation.

3.9. Proposed Fabrication Pathway for the SPR Sensor

Figure 13 presents a conceptual fabrication pathway for the proposed SPR sensor. This scheme is intended to illustrate the planned assembly sequence for future experimental development and should not be interpreted as evidence of device fabrication or validation in the present study. The proposed route begins with the optical prism substrate, followed by deposition of the Al plasmonic layer. An Al_2O_3 coating is then introduced over the Al film to act as a dielectric and protective layer. The WS_2 layer is subsequently placed at the sensing interface to modify the evanescent field and support stronger interaction with the analyte-containing medium. In the final configuration, the milk sample containing H_2O_2 is brought into contact with the WS_2 surface, where concentration-dependent refractive-index changes are expected to induce shifts in the SPR angle.

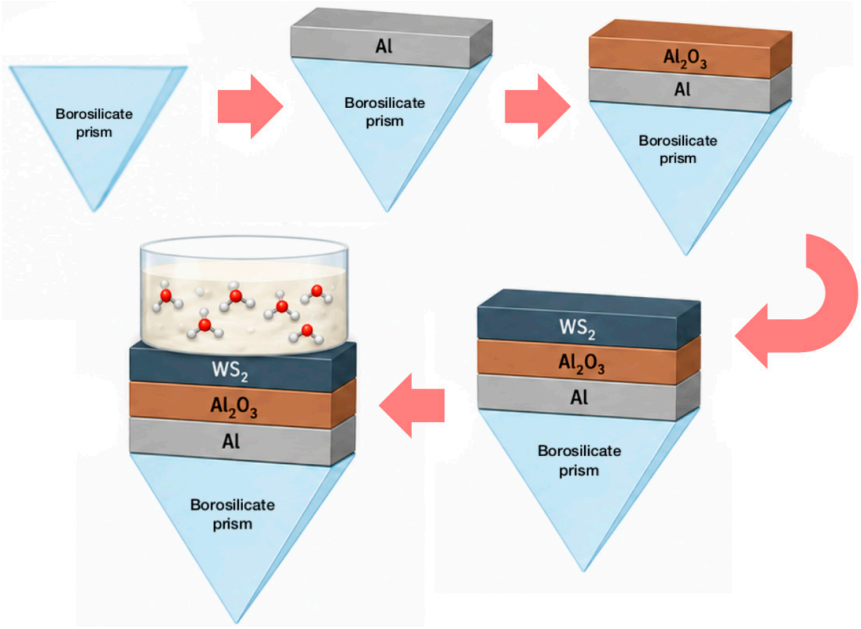


Figure 13. Conceptual fabrication pathway proposed for future development of the SPR sensor, showing sequential assembly of the prism substrate, Al layer, Al_2O_3 coating, WS_2 layer, and milk/H_2O_2 sensing medium.

This assembly route provides a practical basis for translating the numerical design into an experimental platform. Future validation should include controlled thin-film deposition, thickness and roughness characterization, optical alignment under angular interrogation, and testing with milk samples containing known H_2O_2 concentrations. Additional experiments will be required to evaluate repeatability, stability of the Al/Al_2O_3

interface, WS_2 layer uniformity, matrix effects from real milk samples, and selectivity against other possible adulterants or interfering compounds.

3.10. Limitations and Scalability of the Proposed Sensor

The present study is theoretical, so the results should be interpreted within the assumptions of the transfer matrix model. The simulations considered flat, continuous, and optically uniform layers with fixed refractive indices and thicknesses. In a fabricated sensor, film roughness, thickness deviations, interface quality, Al oxidation, and WS_2 coverage may change the resonance angle, attenuation, and FWHM. These nonidealities may produce deviations between the calculated SPR response and the response of a fabricated multilayer, particularly in resonance position, minimum reflectance, and resonance linewidth.

The sensing response was modeled through refractive-index changes associated with H_2O_2 in milk. This approach characterizes the theoretical optical response of the B-sil/Al/Al_2O_3/WS_2 configuration, but it does not include a selective chemical-recognition layer. Real milk contains proteins, lipids, lactose, salts, and other possible adulterants that may also modify the refractive index. Experimental validation is therefore required to confirm selectivity toward H_2O_2.

A second limitation is the broad resonance profile of the selected configuration. Although the configuration shows calculated sensitivity values between 383.82 and 406.45°/RIU, the QF and DA remain lower than some reported SPR platforms. Future optimization should focus on reducing the FWHM while preserving the H_2O_2-dependent angular shift.

From a scalability perspective, the multilayer architecture is compatible, in principle, with planar thin-film fabrication because it uses an Al plasmonic layer, an Al_2O_3 protective coating, and a WS_2 interfacial layer. Future work should fabricate the multilayer stack, verify thickness and surface uniformity, calibrate the sensor with reference liquids, and test real milk samples containing known H_2O_2 concentrations. Selectivity studies against other adulterants will also be needed before practical application.

4. Conclusions

This theoretical study evaluated the angular SPR response of a B-sil/Al/Al_2O_3/WS_2 multilayer configuration to refractive-index variations associated with H_2O_2 in milk under TM-polarized illumination at λ = 633 nm. The multilayer architecture was established through sequential evaluation of prism material, Al thickness, Al_2O_3 thickness, and 2D interfacial material. This procedure led to the selection of B-sil glass, 70 nm Al, 25 nm Al_2O_3, and 0.80 nm WS_2 as the working configuration for analysis of the H_2O_2-associated refractive-index range.

Across the simulated H_2O_2 cases, the resonance angle increased from 85.65° to 86.11° as the refractive index of the sensing medium changed. The calculated angular sensitivity ranged from 383.82 to 406.45°/RIU. The best balance among the evaluated metrics was obtained for H_2O_2-C2, with S = 406.45°/RIU, QF = 4.65 RIU^{-1}, FoM = 436.48 RIU^{-1}, LoD = 1.23 $\times$ 10^{-5}, and CSF = 436.56. The electric-field analysis also showed field localization near the WS_2/sensing-medium interface, consistent with the angular response obtained from the multilayer model.

The systematic assessment of the B-sil/Al/Al_2O_3/WS_2 architecture provides a design-oriented evaluation of this material combination for angular SPR monitoring of H_2O_2-associated refractive-index changes in milk. Comparison with reported SPR systems for milk-related sensing showed a comparable angular sensitivity range, while the broad resonance profile limited QF and detection accuracy. These results describe the theoretical optical behavior of the proposed structure and do not demonstrate chemical selectivity toward H_2O_2. Experimental implementation would require fabrication of the multilayer

stack, calibration with reference liquids and real milk samples, and incorporation of an appropriate selective filtering or recognition strategy to distinguish H_2O_2 from other constituents or adulterants that may produce similar refractive-index variations.

Supplementary Materials: The following supporting information can be downloaded at: https://www.mdpi.com/article/10.3390/bios16090494/s1, Figure S1: Validation of a Numerical Modeling Approach Using Experimental Results from Ref. [38]; Table S1: Code definitions and layer descriptions for the prism-selection study; Table S2: Code definitions and layer descriptions for the aluminum-thickness optimization study; Table S3: Code definitions and layer descriptions for the Al_2O_3-thickness optimization study; Table S4: Optical parameters used for the borosilicate/Al/Al_2O_3/sensing-medium structure at λ = 633 nm; Table S5: Code definitions and layer descriptions for the 2D interfacial-material study; Table S6: Optical parameters used for the borosilicate/Al/Al_2O_3/2D-material/sensing-medium structures at λ = 633 nm; Table S7: Code definitions and layer descriptions for the H_2O_2 concentration study; Table S8: Optical parameters used for the optimized borosilicate/Al/Al_2O_3/WS_2/sensing medium structure at λ = 633 nm.

Author Contributions: J.G.V.L.: Conceptualization, funding acquisition, Writing—original draft. M.G.: Supervision, Conceptualization, Investigation. D.C.-F.: Supervision, Conceptualization, Investigation. C.V.G.: Conceptualization, Software, Methodology, Writing—original draft. All authors have read and agreed to the published version of the manuscript.

Funding: The APC was funded by Universidad de las Fuerzas Armadas (ESPE).

Institutional Review Board Statement: Not applicable.

Informed Consent Statement: Not applicable.

Data Availability Statement: Data presented in this study are available upon reasonable request from the corresponding author.

Acknowledgments: The authors thank the Universidad de las Fuerzas Armadas (ESPE) and ESPOCH for providing lab facilities and resources. The author(s) declared that Generative AI was used in the creation of this manuscript. The authors used ChatGPT 5.2 and Grammarly PRO (v.1.2.279) to improve English. ChatGPT 5.5 was used to create Scheme 1, Figure 13. The prompts to generate these images have been provided as Supplementary material.

Conflicts of Interest: The authors declare no conflicts of interest.

References

1. Kourkouta, L.; Frantzana, A.; Koukourikos, K.; Iliadis, C.; Papathanasiou, I.V.; Tsaloglidou, A. Milk nutritional composition and its role in human health. *J. Pharm. Pharmacol.* **2021**, *9*, 8–13. [CrossRef] [PubMed]
2. Chandan, R.C. Role of milk and dairy foods in nutrition and health. In *Dairy Processing and Quality Assurance*; Chandan, R.C., Kilara, A., Shah, N.P., Eds.; Chapter 18; Wiley: Hoboken, NJ, USA, 2015. [CrossRef]
3. Park, Y.W.; Haenlein, G.F.W. (Eds.) *Milk and Dairy Products in Human Nutrition: Production, Composition and Health*; Wiley: Hoboken, NJ, USA, 2013; 728p, ISBN 978-1-118-53420-5.
4. Pathan, M.M. Physiochemical Properties of Milk. In *Handbook of Milk Production, Quality and Nutrition*; Academic Press: Cambridge, MA, USA, 2025; pp. 35–41. [CrossRef]
5. Chambers, J.V. The microbiology of raw milk. In *Dairy Microbiology Handbook: The Microbiology of Milk and Milk Products*, 3rd ed.; Robinson, R.K., Ed.; Chapter 2; John Wiley & Sons, Inc.: New York, NY, USA, 2002.
6. Sadowska-Bartosz, I.; Bartosz, G. Hydrogen Peroxide: A Ubiquitous Component of Beverages and Food. *Int. J. Mol. Sci.* **2025**, *26*, 3397. [CrossRef] [PubMed]
7. Das, U.; Biswas, R.; Mazumder, N. Quantifying Hydrogen Peroxide in Cattle Milk via a Novel Plasmonic Nanofilm. *ACS Omega* **2025**, *10*, 21786–21794. [CrossRef] [PubMed]
8. Palsoniya, S.; Lal, B.; Mukherji, S. Amperometry Sensor for Real Time Detection of Hydrogen Peroxide Adulteration in Food Samples. *Electrochim. Acta* **2023**, *462*, 142724. [CrossRef]
9. Mohd Arnuar, A.Z.; Nordin, N.; Tajuddin, H.A.; Abdullah, Z. Current Methods for Peroxide Detection in Food and the Emerging Role of Heteroaromatic Dyes as an Efficient Alternative. *J. Food Compos. Anal.* **2024**, *131*, 106191. [CrossRef]

10. Choudhary, M.; Sharma, N. Milk Adulterants: Serious Impact on Human Health. *J. Med. Evid.* **2024**, *5*, 124–128. [CrossRef] [PubMed]
11. Vasconcelos, H.; Matias, A.; Mendes, J.; Araújo, J.; Dias, B.; Jorge, P.A.S.; Saraiva, C.; de Almeida, J.M.M.M.; Coelho, L.C.C. Compact Biosensor System for the Quantification of Hydrogen Peroxide in Milk. *Talanta* **2023**, *253*, 124062. [CrossRef]
12. Aurand, L.W.; Woods, A.E.; Wells, M.R. Food deterioration, preservation, and contamination. In *Food Composition and Analysis*; Springer: Dordrecht, The Netherlands, 1987; pp. 621–663. [CrossRef]
13. Schadt, I. Health Concerns about Possible Long-Term Effects of Legally Marketed Milk and Dairy from Animals with Intramammary Infections. *Front. Public Health* **2023**, *11*, 1200924. [CrossRef] [PubMed]
14. Prokopov, T.; Tanchev, S. Methods of food preservation. In *Food Safety*; McElhatton, A., Marshall, R.J., Eds.; Springer: Boston, MA, USA, 2007; Volume 1. [CrossRef]
15. Szczęsny, G.; Kopeć, M.; Kowalewski, Z.L. Toxicity, Irritation, and Allergy of Metal Implants: Historical Perspective and Modern Solutions. *Coatings* **2025**, *15*, 361. [CrossRef]
16. Sangubotla, R.; Mastan, A.; Kim, J. Recent Advances in Electrochemical Biosensors for the Detection of Milk Adulterants. *Biosensors* **2026**, *16*, 92. [CrossRef] [PubMed]
17. Joolaei Ahranjani, P.; Dehghan, K.; Esfandiari, Z.; Joolaei Ahranjani, P. A Systematic Review of Spectroscopic Techniques for Detecting Milk Adulteration. *Crit. Rev. Anal. Chem.* **2026**, *56*, 1071–1102. [CrossRef] [PubMed]
18. Silva, A.F.S.; Rocha, F.R.P. A novel approach to detect milk adulteration based on the determination of protein content by smartphone-based digital image colorimetry. *Food Control* **2020**, *115*, 107299. [CrossRef]
19. Sen, S.; Donthula, H.; Ravindar, B.; Jala, S.; Mitta, C.; Kalepu, S. Qualitative and Quantitative Analysis for Adulteration and Nutritional Value of Milk: A Case Study. *Neuroquantology* **2022**, *20*, 227–237. [CrossRef]
20. Sharma, A.; Yadav, M.; Kumar, N.; Chandu, G.; Jana, R.; Pandey, P.; Kumar, R. Rapid Detection of Milk Adulteration Using AI-Driven Portable Colorimetric Spectroscopy. *Discov. Food* **2026**. [CrossRef]
21. Yadav, A.K.; Gattupalli, M.; Dashora, K.; Kumar, V. Key Milk Adulterants in India and Their Detection Techniques: A Review. *Food Anal. Methods* **2023**, *16*, 499–514. [CrossRef]
22. Ng, P.C.; Khor, S.M. Optical Detection of Targets for Food Quality Assessment. In *Biosensing and Micro-Nano Devices*; Chandra, P., Ed.; Springer: Singapore, 2022; pp. 121–167. [CrossRef]
23. Periyasamy, A.; Selvam, S.; Chellakannu, A.; Sivasamy, V.V.; Mariakuttikan, J. Electrochemical Sensors for the Detection of Food Adulterants in Miniaturized Settings. In *Nanosensing and Bioanalytical Technologies in Food Quality Control*; Chandra, P., Panesar, P.S., Eds.; Springer: Singapore, 2022; pp. 139–168. [CrossRef]
24. Vigolo, V.; Niero, G.; Penasa, M.; De Marchi, M. Effects of Preservative, Storage Time, and Temperature of Analysis on Detailed Milk Protein Composition Determined by Reversed-Phase High-Performance Liquid Chromatography. *J. Dairy Sci.* **2022**, *105*, 7917–7925. [CrossRef] [PubMed]
25. Hemmateenejad, B.; Ardakani, F. Optical Sensor Arrays for Food Adulteration Detection. In *Advanced Techniques against Food Adulteration*; Alahmad, W., Ashfaq, M., Eds.; Springer: Cham, Switzerland, 2025; pp. 159–189. [CrossRef]
26. Chugh, R.; Kaur, G. A Study on Milk Adulteration and Methods of Detection of Various Chemical Adulterants Qualitatively. *IOP Conf. Ser. Mater. Sci. Eng.* **2022**, *1225*, 012046. [CrossRef]
27. Kumar, M. *Laboratory Manual of Milk Testing*; Manoj Kumar: Jhansi, India, 2025; 197p, ISBN 9798269309972.
28. Dhar, P.; Bhowmik, A.; Nath, P.C.; Patel, D.; Shankar, A.; Tomar, P.; Sinha, A. Smart technologies in food safety and quality monitoring: A review of technological advances, opportunities and challenges. *J. Food Process Eng.* **2026**, *49*, e70367. [CrossRef]
29. Peveler, W.J. Food for Thought: Optical Sensor Arrays and Machine Learning for the Food and Beverage Industry. *ACS Sens.* **2024**, *9*, 1656–1665. [CrossRef] [PubMed]
30. Harini, V.K.; Meher, S.R.; Alex, Z.C. A Novel Refractive Index Based-Fiber Optic Sensor for Milk Adulteration Detection. *Opt. Mater.* **2024**, *154*, 115810. [CrossRef]
31. Sharma, V.; Dwivedi, L.K.; Singh, S.K. Graphene-Coated Surface Plasmon Resonance (SPR) Sensor for Detection of Preservatives in Milk: A Theoretical Investigation. *Int. J. Sci. Res. Sci. Technol.* **2023**, *10*, 256–266. [CrossRef]
32. Das, U.; Biswas, R. Advances in Plasmonic Nanoprobes for Sensitive Detection of Key Milk Adulterants: A Comprehensive Review. *Microchem. J.* **2025**, *218*, 115543. [CrossRef]
33. Ahamed, S.; Venkatesan, K.K.; Jalaludeen, S.A. A Review on Various Surface Plasmon Resonance-Based Sensors. *Plasmonics* **2025**, *20*, 6869–6885. [CrossRef]
34. Chen, T.; Xin, J.; Chang, S.J.; Chen, C.-J.; Liu, J.-T. Surface Plasmon Resonance (SPR) Combined Technology: A Powerful Tool for Investigating Interface Phenomena. *Adv. Mater. Interfaces* **2023**, *10*, 2202202. [CrossRef]
35. Roy, D. Optical characterization of multi-layer thin films using the surface plasmon resonance method: A six-phase model based on the Kretschmann formalism. *Opt. Commun.* **2001**, *200*, 119–130. [CrossRef]
36. Simone, G. Proof of Enantioselectivity in a Multilayer with a Strong Exciton Polariton Coupling and through Asymmetric Polarization. *arXiv* **2023**, arXiv:2309.08979. [CrossRef]

37. Tene, T.; Villacres Cevallos, E.P.; Palacios Robalino, M.L.; Caputi, L.S.; Straface, S.; Vacacela Gomez, C. Surface Plasmon Resonance and Reduced Graphene Oxide for Optical Ion Monitoring in Water: A Numerical Modeling. *Photonics* **2025**, *12*, 1162. [CrossRef]
38. Cheon, S.; Kihm, K.D.; Kim, H.G.; Lim, G.; Park, J.S.; Lee, J.S. How to reliably determine the complex refractive index (RI) of graphene by using two independent measurement constraints. *Sci. Rep.* **2014**, *4*, 6364. [CrossRef] [PubMed]
39. Solis-Tinoco, V.; Morales-Luna, G.; Acevedo-Barrera, A.; Ochoa, A.; Vazquez-Estrada, O.; Olguin, L.F.; García-Valenzuela, A. An Optical Sensor Combining Surface Plasmon Resonance, Light Extinction, and Near-Critical Angle Reflection, for Thin Liquid Film Biochemical Sensing. *Opt. Lasers Eng.* **2022**, *158*, 107137. [CrossRef]
40. Liu, L.; Liu, Z.; Zhang, Y.; Liu, S. Multi-channel optical fiber surface plasmon resonance sensor with narrow FWHM, high figure of merit, and wide detection range. *Plasmonics* **2022**, *17*, 2235–2244. [CrossRef]
41. Ansari, M.T.I.; Raghuwanshi, S.K.; Kumar, S. Recent Advancement in Fiber-Optic-Based SPR Biosensor for Food Adulteration Detection—A Review. *IEEE Trans. Nanobiosci.* **2023**, *22*, 978–988. [CrossRef] [PubMed]
42. Alexandros, G.K.; Nikolaos, S.; Dimitris, A.; Alexandros, A.V.; George, D.P. Nanoporous alumina enhanced surface plasmon resonance sensors. *J. Appl. Phys.* **2008**, *103*, 094521. [CrossRef]
43. Li, W.; Ren, K.; Zhou, J. Aluminum-based localized surface plasmon resonance for biosensing. *TrAC Trends Anal. Chem.* **2016**, *80*, 486–494. [CrossRef]
44. Sadeghi, S.; Mohammadimasoudi, M.; Mehrzad, H.; Goudarzi, A. Hydrogen peroxide and glucose detection using surface plasmon resonance imaging biosensor with corrodible silver thin film. *Talanta* **2024**, *279*, 126593. [CrossRef] [PubMed]
45. Pham, X.-H.; Seong, B.; Bock, S.; Hahm, E.; Huynh, K.-H.; Kim, Y.-H.; Kim, W.; Kim, J.; Kim, D.-E.; Jun, B.-H. Nonenzymatic hydrogen peroxide detection using surface-enhanced Raman scattering of gold–silver core–shell-assembled silica nanostructures. *Nanomaterials* **2021**, *11*, 2748. [CrossRef] [PubMed]
46. Parisi, A.; Cino, A.C.; Busacca, A.C.; Cherchi, M.; Riva-Sanseverino, S. Integrated Optic Surface Plasmon Resonance Measurements in a Borosilicate Glass Substrate. *Sensors* **2008**, *8*, 7113–7124. [CrossRef] [PubMed]
47. Tene, T.; Polanco, M.A.; Caputi, L.S.; Straface, S.; Vacacela Gomez, C. Design and Numerical Optimization of a Borosilicate-Supported Aluminum SPR Sensor for Monitoring Metal Ion Mixtures. *Opt. Commun.* **2026**, *616*, 133372. [CrossRef]
48. Srivastava, A.; Agarwal, S. Enhancement of Dynamic Range of Surface Plasmon Resonance (SPR) Biosensor Using High Refractive Index Prism: A Theoretical Approach. In *Opto-VLSI Devices and Circuits for Biomedical and Healthcare Applications*; CRC Press: Boca Raton, FL, USA, 2023; 10p.
49. Sayed, M.; Yu, J.; Liu, G.; Jaroniec, M. Non-Noble Plasmonic Metal-Based Photocatalysts. *Chem. Rev.* **2022**, *122*, 10484–10537. [CrossRef] [PubMed]
50. Domanowska, A.; Adamowicz, B. Auger Electron Spectroscopy for Chemical Analysis of Passivated (Al,Ga)N-Based Systems. *Micromachines* **2026**, *17*, 47. [CrossRef] [PubMed]
51. Awad, H.D.; Aljbar, N.A.; Khalid, A.H.; Jabor, A.A.H.; Ali, K.A.M.; Khalaf, M.K.; Yaseen, S.F. Construction Surface Plasmon Resonance Sensor System of a Bilayer Au/Aluminum Oxide for Gas Sensing Application. *AIP Conf. Proc.* **2026**, *3460*, 050003. [CrossRef]
52. Ghodrati, M.; Mir, A.; Farmani, A. Sensitivity-Enhanced Surface Plasmon Resonance Sensor with Bimetal/Tungsten Disulfide (WS_2)/MXene (Ti3C2Tx) Hybrid Structure. *Plasmonics* **2022**, *17*, 1973–1984. [CrossRef]
53. Niknam, S.; Dehdast, S.A.; Pourdakan, O.; Shabani, M.; Koohi, M.K. Tungsten Disulfide Nanomaterials (WS_2 NM) Application in Biosensors and Nanomedicine: A Review. *Nanomed. Res. J.* **2022**, *7*, 214–226. [CrossRef]
54. Bin Abdul Akib, T.; Rana, M.M.; Mehedi, I.M. Multi-Layer SPR Biosensor for In-Situ Amplified Monitoring of the SARS-CoV-2 Omicron (B.1.1.529) Variant. *Biosens. Bioelectron. X* **2024**, *16*, 100434. [CrossRef]
55. Ghosh, S.; Preza, C. Characterization of a Three-Dimensional Double-Helix Point-Spread Function for Fluorescence Microscopy in the Presence of Spherical Aberration. *J. Biomed. Opt.* **2013**, *18*, 036010. [CrossRef] [PubMed]
56. Saracoglu, O.G.; Hayber, S.E. Bent Fiber Sensor for Preservative Detection in Milk. *Sensors* **2016**, *16*, 2094. [CrossRef] [PubMed]
57. Sayed, F.A.; Elsayed, H.A.; Al-Dossari, M.; Eissa, M.F.; Mehaney, A.; Aly, A.H. Angular Surface Plasmon Resonance-Based Sensor with a Silver Nanocomposite Layer for Effective Water Pollution Detection. *Sci. Rep.* **2023**, *13*, 21793. [CrossRef] [PubMed]
58. Singh, S.K.; Srivastava, A.; Dwivedi, L.K. A Theoretical Analysis of Milk Adulteration/Contamination Detection in Camel, Buffalo and Cow Milk Using SPR Technique. *J. Phys. Conf. Ser.* **2023**, *2426*, 012040. [CrossRef]
59. Paswan, M.K.; Basu, R. Surface Plasmon Resonance Sensor for Milk Adulteration Detection Using a CaF2 Prism, Ag Film, and Black Phosphorus Layer. *Micro Nano Struct.* **2025**, *205*, 208193. [CrossRef]
60. Anjali, C.C.; Vasimalla, Y.; Srither, S.R.; Ramachandran, B.; Santhosh, C.; Babu, K.; Kumar, S. A Novel Approach for Enhanced Detection of Fat Concentration in Milk Using a Label-Free Nano Biosensor Employing Barium and Cadmium Gallium Sulfide. *Plasmonics* **2025**, *20*, 9309–9321. [CrossRef]

Disclaimer/Publisher's Note: The statements, opinions and data contained in all publications are solely those of the individual author(s) and contributor(s) and not of MDPI and/or the editor(s). MDPI and/or the editor(s) disclaim responsibility for any injury to people or property resulting from any ideas, methods, instructions or products referred to in the content.